2018

Phonon Transport at Boundaries and Interfaces in Two-Dimensional Materials

Cameron Foss

Recommended Citation

Foss, Cameron, "Phonon Transport at Boundaries and Interfaces in Two-Dimensional Materials" (2018). *Masters Theses*. 686.
https://scholarworks.umass.edu/masters_theses_2/686

PHONON TRANSPORT AT BOUNDARIES AND INTERFACES IN TWO-DIMENSIONAL MATERIALS

A Thesis Presented

by

CAMERON J. FOSS

Submitted to the Graduate School of the
University of Massachusetts Amherst in partial fulfillment
of the requirements for the degree of

MASTER OF SCIENCE IN ELECTRICAL AND COMPUTER ENGINEERING

September 2018

Electrical and Computer Engineering

PHONON TRANSPORT AT BOUNDARIES AND INTERFACES IN TWO-DIMENSIONAL MATERIALS

A Thesis Presented

by

CAMERON J. FOSS

Approved as to style and content by:

Zlatan Aksamija, Chair

Neal Anderson, Member

Eric Polizzi, Member

Christopher V. Hollot, Department Head
Electrical and Computer Engineering

DEDICATION

To my family.

ACKNOWLEDGMENTS

I would like to extend the utmost respect and gratitude to my advisor Prof. Zlatan Aksamija for his guidance and support. I would like to thank Prof. Anderson and Prof. Polizzi for serving as my review committee. I would also like to thank my family and friends for their unwaivering support.

ABSTRACT

PHONON TRANSPORT AT BOUNDARIES AND INTERFACES IN TWO-DIMENSIONAL MATERIALS

SEPTEMBER 2018

CAMERON J. FOSS
B.S., UNIVERSITY OF MASSACHUSETTS AMHERST
M.S.E.C.E., UNIVERSITY OF MASSACHUSETTS AMHERST

Directed by: Professor Zlatan Aksamija

A typical electronic or photonic device may consist of several materials each one potentially meeting at an interface or terminating with a free-surface boundary. As modern device dimensions reach deeper into the nanoscale regime, interfaces and boundaries become increasingly influential to both electrical and thermal energy transport. While a large majority of the device community focuses on the former, we focus here on the latter issue of thermal transport which is of great importance in implementing nanoscale devices as well as developing solutions for on-chip heat removal and waste heat scavenging. In this document we will discuss how modern performance enhancing techniques (strain, nanostructuring, alloying, etc.) affect thermal transport at boundaries and across interfaces through the avenue of three case studies. We use first-principles Density Functional Perturbation Theory to obtain the phonon spectrum of the materials of interest and then use the dispersion data as input to a phonon Boltzmann Transport model. First, we investigate the combined effects of strain and boundary scattering on the in-plane and cross-plane thermal conductivity of thin-film silicon and germanium. Second, we review a recently developed model for cross-dimensional (2D-3D) phonon transport and apply it to 3D-2D-3D stacked interfaces involving graphene and molybdenum disulfide 2D-layers. Third, we combine relevant models from earlier Chapters to study extrinsic effects, such as line edge roughness and substrate effects, on in-plane and through-plane thermal transport in 1H-phase transition metal dichalcogenide (TMD) alloys. Through these investigations we show that: (1) biaxial strain in Si and Ge thin-films can modulate cross-plane conductivity due to strong boundary scattering, (2) the thermal boundary conductance between 2D-3D materials can be enhanced in the presence of an encapsulating layer, and (3) the thermal conductivity of 1H-phase TMDs can be reduced by an order of magnitude through the combination of nanostructuring, alloying, and substrate effects.

TABLE OF CONTENTS

LIST OF FIGURES

CHAPTER 1

INTRODUCTION

1.1 Overview

The field of nanotechnology comes with equal parts excitement and fundamental challenges. Nanomaterials exhibit the potential to enable a plethora of novel or improved devices with new or enhanced functionalities that can be exploited to innovate next-generation technologies. However, one prominent issue that has plagued the progression of electronic devices and hinders the implementation of nanostructures is heat dissipation [85]. Poor management of thermal waste heat can interfere with a devices intended application and accelerate degradation, shortening device lifetime [71]. At the nanoscale, phonon collisions with rough boundaries and interfaces between dissimilar materials of varying morphologies become additional sources of resistance perpetuating thermal transport problems [13, 15, 85]. For these reasons, there has been a revived interest in the study and characterization of the thermal conductivity (κ) of semiconductor crystals, their nanostructured counterparts, and their interfaces.

While there has been tremendous advancements in the growth and fabrication of nanostructured materials, the ability to reliably grow high-quality single-crystal nanostructures in large quantities remains a topic of intense research [32, 64, 24]. As a consequence, the variability of sample preparation and/or quality can often be reflected in experimental measurements giving rise to issues of reproducibility and definitive trends [91, 114]. Moreover, experimental measurements of nanostructures present new challenges due to the sensitivity of nanomaterials to their environment, the resolution of measurement equipment, and the difficulties in determining the details of transport near boundaries and across interfaces. Thus it is important to develop and implement theoretical models in parallel with experiments to help deconvolve physical measurements, provide fundamental insight, and to find qualitative trends.

In this work, we focus on phonon transport near the boundaries and interfaces of two-dimensional nanostructures within the scope of modern engineering design tactics such as strain, dimension downscaling, and alloying. For most materials, we obtain the full phonon spectrum from first-principles Density Functional Perturbation Theory (DFPT) simulations from which we can calculate phonon group velocities and vibrational density of states. With the full phonon spectrum, we can then calculate thermal transport within a material using the phonon Boltzmann Transport Equation, or we can calculate transport across an interface using a typical Landauer formalism. In the next section, we will introduce relevant background for our case studies.

1.2 Relevant Background

In most solids and some liquids, atoms bonded by strong or weak forces vibrate amongst themselves leading to collective excitations often referred to as phonons. In relevant electronic materials, thermal currents are driven by both electrons and phonons. For metals, thermal currents are typically dominated by the high concentration of electrons which tend to dominate the total thermal conductivity taken as the sum of the phonon and electron parts – $\kappa_{tot} = \kappa_{ph} + \kappa_{el}$. In semiconductors at moderate doping concentrations, the thermal conductivity is typically dominated by the phonon contribution, often termed the lattice thermal conductivity. In this body of work, we will restrict our scope to phonon transport alone.

Lattice thermal conductivity κ_L in bulk semiconductors is governed by three-phonon Normal (non-resistive) and Umklapp (resistive) processes [34]. When sample dimensions are reduced to the nanoscale (a few to 100s of nm) phonon collisions with boundaries give rise to boundary scattering which can often reduce the thermal conductivity by an order of magnitude or more [3, 70]. In very small samples (<10s of nm) the surface (or edge) patterning and roughness height can further influence thermal transport – boundaries/edges that have very rough features scatter phonons more diffusely (reducing κ_L) while smooth features scatter phonons more specularly, having little to no effect on κ_L [68, 7].

In the case of alloyed materials, mass-difference scattering arises and typically becomes the new dominant scattering mechanism [35]. Phonons can also collide with isotopes, impurities and lattice defects or disorder. In general, the concentration of isotopes and impurities strongly determines their influence – however, very large concentrations are often needed in order for isotope or impurity scattering to overcome other scattering mechanisms, such as boundary and mass-difference scattering [101, 73, 70]. Concentration also plays an important role with defect scattering, although the topology of defects can largely affect its influence on κ_L and is also a subject of intense research [25, 47, 55, 115].

To this point, the scattering mechanisms mentioned generally occur within a single grain of a material, where a grain is defined as a region having a single-crystalline structure. However, practical devices are often composed of several materials, each having different electrical (metal, semiconductor, insulator) and thermal (low to high κ_L) properties, and the interface formed at the meeting point between any two material domains introduces an additional component of resistance to thermal transport [13, 15, 46]. The influence of material interfaces on overall device thermal resistance varies depending on grain size, the topology of the interface (rough and disordered or smooth and well-structured), the type of atomic bonding at the interface (strong covalent or weak van der Waals bonding), the acoustic impedance of each grain, and the distribution of available phonon states between the two domains [45, 46].

In modeling phonon transmission across the interface of two material domains, there are two long-standing models – the Diffuse Mismatch Model [96, 97] (DMM) and the Acoustic Mismatch Model [62] (AMM). In the DMM, it is assumed that all phonons scatter at the interface, which best represents interfacical transport at high temperatures or across interfaces with significant roughness and defects. In the AMM, it is assumed that there is no scattering of phonons crossing the interface, which has been shown to best fit experimental measurements at low temperatures or involving interfaces with smooth, coherent interfaces. Either model seldom fits experimental measurements perfectly across all temperatures, but instead act as two extremes giving lower (DMM) and upper (AMM) bounds for the thermal boundary conductance. We introduce the topics of these scattering mechanisms here as they forshadow relevant discussions in the following chapters.

1.3 Outline of Thesis

The remainder of this document is organized as follows: Chapter 2 discusses how strain affects cross-plane thermal transport in thin-films of group IV semiconducting Silicon and Germanium. Chapter 3 briefly reviews a recently developed cross-dimensional (2D-3D) interface transport model and implements it to study metal-monolayer-substrate stacked systems. We then investigate the role of extrinsic scattering mechanisms on phonon transport in transition metal dichalcogenide 2D alloys in Chapter 4.

CHAPTER 2

STRAIN EFFECTS ON IN-PLANE AND CROSS-PLANE THERMAL TRANSPORT IN SI AND GE THIN FILMS

We begin our study by investigating thermal transport in thin-films of strained silicon and germanium where boundary scattering is the dominant scattering mechanism. We augment previous studies on various strained silicon systems with our calculations of both in-plane (IP) and cross-plane (CP) thermal conductivity, performed with the pBTE, focusing on Si and Ge thin films under both compressive and tensile biaxial strain and with film thickness varying across six orders of magnitude. The full phonon dispersion of Si and Ge under ± 4% (tensile/compressive) biaxial strain is calculated from first-principles Density Functional Perturbation Theory [12]. While our results confirm weak strain dependence in silicon and germanium thin films for IP thermal transport, we uncover a much stronger strain dependence in the CP direction. We provide an explanation on where this strain-dependence discrepancy between IP and CP transport originates through our momentum-dependent boundary scattering model. In 20 nm films at room temperature, we show that 4% strain results in a large ∼20% variation in the CP conductivity, with tensile strain decreasing and compressive strain increasing the conductivity. Since IP conductivity remains relatively unaffected, we also observe an increase (decrease) with tensile (compressive) strain in the anisotropy between IP and CP transport. Our results indicate that strain may be an effective tool for modulating the cross-plane thermal conductivity in thin-films for efficient heat removal from strained Si/SOI and Ge/GOI devices.

2.1 Overview of strain in Si-based nanostructures

Thermal conductivity of strained silicon-based nanostructures has been studied theoretically [110, 60, 78, 119] and experimentally [73]. Xu and Li [110] studied cross-plane thermal transport in uniaxially and hydrostatically strained two-dimensional nanocomposites consisting of Si nanowires (NWs) embedded in Ge. They performed lattice dynamics calculations including strain, coupled to a phonon Boltzmann transport equation (pBTE) solver with diffuse NW boundaries, and found a large strain dependence in the cross-plane (along the embedded NWs) in $Si_{0.2}Ge_{0.8}$ nanocomposites under hydrostatic strain. Yang *et al.* [60] studied the strain effects on thermal conductivity in silicon NWs and thin films as well as single-walled carbon nanotubes and two-dimensional graphene. They performed Equilibrium Molecular Dynamics (EMD) simulations to calculate the thermal conductivity (κ) which employs a numerical surface reconstruction method to account for surface interactions. Their results show κ decreases monotonically from compressive to tensile strain in Si and diamond thin films and NWs.

Paul and Klimeck [78] studied the ballistic thermal transport in NWs under hydrostatic and uniaxial strains using a modified Valence Force Field (VFF) approach to calculate the phonon dispersion. For hydrostatic compressive/tensile strains, they found that thermal conductivity was unaffected. However, for uniaxial strain, a monotonic trend similar to Yang *et al.* was observed. Zhang and Wu performed MD studies of strained Si thin films [119] and also found a modest monotonic strain dependence for transport along the thin film. Murphy *et al.* [73] performed an experimental investigation into uniaxial strain in silicon NWs using a novel piezoelectric Raman Spectroscopy approach. Their findings support a weak strain dependence on heat transport in the direction along the NWs. Despite these studies, comparatively less attention has been devoted to the effect of biaxial strain on thermal transport in thin Si and Ge films, which may impact applications in strain-engineered silicon-on-insulator (sSOI) [1, 29, 54] and strained germanium-on-insulator (sGOI) nanomembrane devices [94, 49], as well as strained Si [43] and Si/Ge superlattice thermoelectrics [19, 56, 48]. Even less attention has been devoted to transport in the direction normal to the thin film/membrane (cross-plane direction), and the anisotropy between transport along and across the film/membrane.

2.2 Methodology

2.2.1 First-principles Simulations

In order to fully capture the effects of strain, we have calculated the phonon dispersion of Si and Ge under compressive and tensile biaxial strains using first-principles Density Functional Perturbation Theory (DFPT). All simulations are performed with the open-source software Quantum-ESPRESSO [37]. Fundamental changes in the mechanical properties of a material can be deduced from observing the phonon dispersion relations. Biaxial strain is applied by fixing the lattice constant in the xy-plane and allowing the out-of-plane (z-plane) lattice constant to relax energetically. Naturally, biaxial strain breaks the cubic symmetry of the face-center cubic lattice.

After the system energy has been minimized a final *self-consistent field* calculation is performed. We use a norm conserving pseudopotential that uses a direct-fit Von Barth-Car method with a Perdew-Zunger (LDA) exchange correlation for Si, and a norm conserving pseudopotential that uses a Goedecker-Hartwigsen-Hutter-Teter method also with a Perdew-Zunger (LDA) exchange correlation for Ge. A 4×4×4 Monkhorst-Pack grid size with a 1×1×1 offset was used with an energy cutoff for plane waves of 16 Ry for Si and 24 Ry for Ge. Conventional lattice constants were used for unstrained cases, 5.431 Å for Si and 5.658 Å for Ge with a convergence threshold of 10^{-9}. After the self-consistent calculation, a phonon calculation is done to obtain dynamical matrices in Fourier space on a 4×4×4 grid and a convergence threshold of 10^{-15}. The dynamical matrices are then inverse Fourier transformed from which phonon frequencies are sampled on a dense grid of 33,200 (232,400) k-points.

In Fig. 2.1 we show the dispersions for silicon and germanium plotted along high-symmetry paths Γ-K-X-Γ-L-X-W-L. A clear increase in optical branch frequencies with compressive strain is seen, with the exception of -2% strain in germanium. For tensile strains, there is a clear decrease in optical phonon frequencies in either material. Similar trends can be seen in previous works on strain effects on phonon dispersions of materials [89, 95, 27]. Branch-wise phonon group velocities are calculated as the gradient of the dispersion, $v_j(\boldsymbol{q}) = \partial\omega_j(\boldsymbol{q})/\partial\boldsymbol{q}$, using a central difference method. Hence the slope of the dispersion curves represents the group velocity of phonons. Optical phonons have low velocities and are high in energy, thus they act as energy storage and do not contribute greatly to heat flow. Conversely, acoustic phonons are high in velocity and are present at much lower temperatures, thus acoustic phonons are the main contributors to thermal transport.

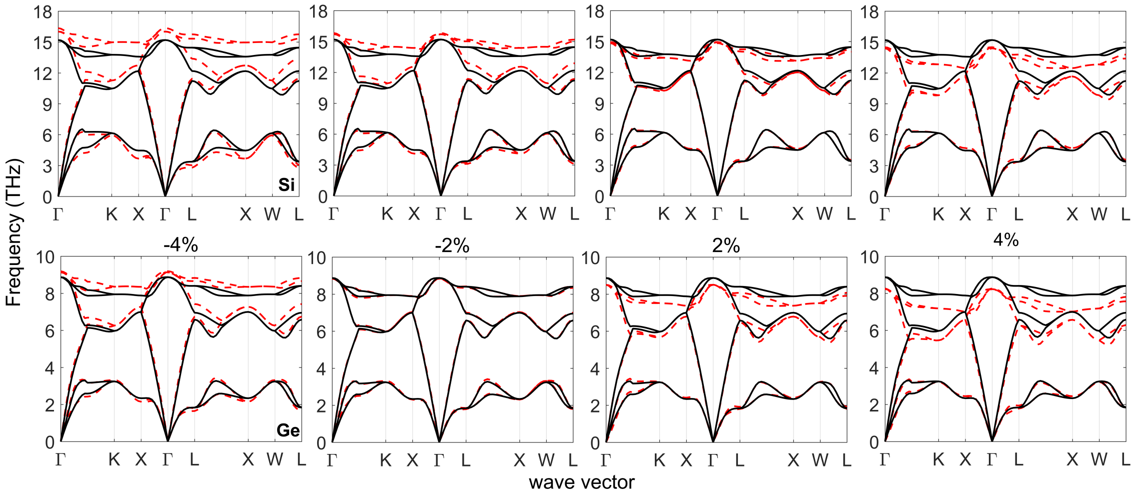

Figure 2.1. The phonon dispersions of unstrained (solid black) and strained (dashed red) silicon (top) and germanium (bottom). The amount of strain increases from -4% to +4% from left to right. The six phonons branches from bottom to top are labeled TA1, TA2, LA, LO, TO1, and TO2 and represent transverse/longitudinal acoustic/optical phonons.

2.2.2 Phonon BTE and intrinsic scattering mechanisms

The thermal properties of silicon nanostructures [4], $\mathrm{Si}_{1-x}\mathrm{Ge}_x/\mathrm{Si}_{1-y}\mathrm{Ge}_y$ superlattices [7], and other SiGe nanostructures [102] have been studied using a phonon Boltzmann transport model with a relaxation time approximation that incorporates intrinsic and extrinsic scattering mechanisms. We extend the use of this model and apply it to strained Si and Ge thin films. The temperature dependent thermal conductivity tensor can be obtained from a summation over all q-vectors $\boldsymbol{q}$ and phonon branches j as

$$\boldsymbol{K}^{\alpha\beta}(T) = k_B \sum_j \sum_{\boldsymbol{q}} C_j(\boldsymbol{q}, T)\tau_j(\boldsymbol{q}) v_j^{\alpha}(\boldsymbol{q}) v_j^{\beta}(\boldsymbol{q}) \ . \tag{2.1}$$

$C_j(\boldsymbol{q}, T)$ is the heat capacity per mode, k_B is the Boltzmann constant, $\tau_j(\boldsymbol{q})$ is the total relaxation time, and $v_j^{\alpha}(\boldsymbol{q})$ is the phonon velocity in the α Cartesian direction. The modal heat capacity can be represented as function of temperature and q-vector

$$C_j(\boldsymbol{q}, T) = \left[\frac{\hbar\omega_j(\boldsymbol{q})}{kT}\right]^2 \frac{e^{\hbar\omega_j(\boldsymbol{q})/kT}}{[e^{\hbar\omega_j(\boldsymbol{q})/kT} - 1]^2} \ . \tag{2.2}$$

The conductivity tensor is diagonal and isotropic in bulk Si and Ge ($\boldsymbol{K}^{xx} = \boldsymbol{K}^{yy} = \boldsymbol{K}^{zz}$) due to cubic symmetry, but in nanostructures such as thin films, boundary scattering and strain can break this symmetry and cause anisotropy [69]. For this reason, the conductivity tensor in thin Si films has been shown to have different components in the IP and CP directions [3].

Our model accounts for isotope (I), internal three-phonon normal (N) and umklapp (U) intrinsic scattering mechanisms. The relation between individual scattering mechanisms and the total intrinsic relaxation time $\tau_{j,int.}(\boldsymbol{q})$ follows

$$\frac{1}{\tau_{j,int.}(\boldsymbol{q})} = \frac{1}{\tau_{j,N}(\boldsymbol{q})} + \frac{1}{\tau_{j,U}(\boldsymbol{q})} + \frac{1}{\tau_{j,I}(\boldsymbol{q})}. \tag{2.3}$$

The temperature driven transition between normal and umklapp scattering processes in bulk Si and Ge is modeled using a general method described by Slack *et al.* [72] and can be written in the following forms,

$$\tau_{j,N}^{-1}(\boldsymbol{q}) = \frac{\gamma_j^2}{M\bar{v}_j^3}\omega_j^2(\boldsymbol{q})Te^{-\Theta_j/3T} \tag{2.4}$$

and

$$\tau_{j,U}^{-1}(\boldsymbol{q}) = \frac{\hbar\gamma_j^2}{M\Theta_j\bar{v}_j^2}\omega_j^4(\boldsymbol{q})Te^{-\Theta_j/3T} \ . \tag{2.5}$$

M is the atomic mass, γ_j is the Grüneisen parameter, $\bar{v}_j$ is the average phonon group velocity of branch j, and Θ_j is the Debye temperature per branch. While these rates are based on an empirical model rather than calculated from first principles, they do not have any adjustable parameters: γ_j, v_j, and Θ_j are all calculated from the phonon dispersion [102] and are not adjustable. Their accuracy is sufficient for the purposes of this work because our focus is on trends in strain dependence in nanostructures such as thin films where boundary scattering, described further in the next section, is dominant. First principles calculations of anharmonic phonon-phonon scattering in Si found the same quadratic dependence of the normal rate [28], but a stronger quartic dependence of the umklapp rate [108], which is matched by our rates. When tensile (compressive) strain is applied, normal and umklapp scattering between acoustic branches, which are the primary contributors to heat flow, have been found to increase (decrease) with the amount of strain.

Scattering with isotopes is elastic; hence, it is related to the vibrational density of states, as described by the following equation [100, 67],

$$\tau_{j,I}^{-1}(\boldsymbol{q}) = \frac{\pi V_0}{6}\Gamma_{Si}\omega^2 D(\omega) \ , \tag{2.6}$$

where V_0 is the volume per atom, $D(\omega)$ is the vibrational density of states, and $\Gamma_{Si} = \sum_i f_i(1 - m_i/\bar{m})^2$, where f_i is the natural abundance of isotope i with mass m_i, and the average mass is $\bar{m} = \sum_i f_i m_i$. The energy-dependent vibrational density of states

$$D(\omega) = \sum_i \int \frac{d\boldsymbol{q}}{(2\pi)^3} \delta[\omega - \omega_j(\boldsymbol{q})] \tag{2.7}$$

is calculated using the Brillouin zone integration method described by Gilat and Raubenheimer [38].

2.2.3 Boundary roughness scattering in thin films

We use a boundary scattering model that determines the specularity of boundary collisions from the surface roughness and angle of phonon wave incidence. This factor describes the probability of a wave phonon reflecting at the boundary; otherwise, the phonon is scattered diffusely, provided it does not scatter internally before reaching the boundary by the intrinsic mechanisms described in the previous section. The specularity of a given collision is determined from the phonon momentum by $p(\boldsymbol{q}) = exp(-4\Delta^2 q^2 cos^2 \Theta_B)$ where Δ is the root-mean-square (rms) surface roughness and Θ_B is the angle of incidence.

The relaxation time for boundary events can be written in the following way,

$$\tau_{j,B}^{-1}(\boldsymbol{q}) = \frac{v_j^{\perp}(\boldsymbol{q})}{H} \frac{F_p(\boldsymbol{q}, H)}{1 - \frac{\tau_{j,int}(\boldsymbol{q}) v_j^{\perp}(\boldsymbol{q})}{H} F_p(\boldsymbol{q}, H)} \ . \tag{2.8}$$

The first term gives a rate determined by the velocity of each phonon and the thickness of the film and the second term determines the specularity of the wave and typically takes values between 0 (purely diffuse) and 1 (purely specular). The relaxation time

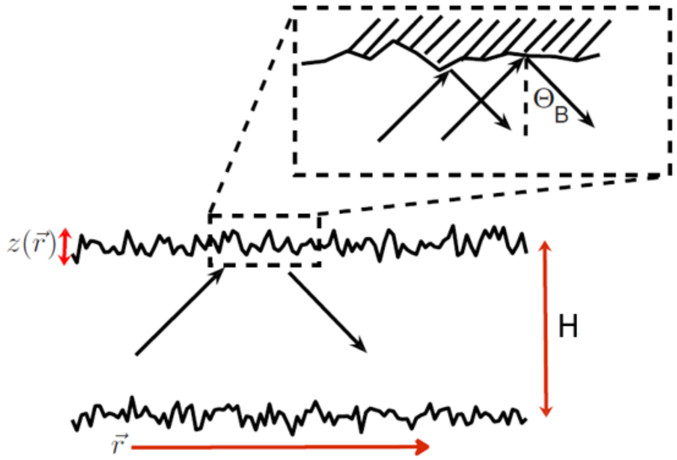

Figure 2.2. An illustration of a phonon colliding with a rough surface of a silicon thin-film. Here H is the film thickness, $\vec{r}$ is the two dimensional position vector along the surface plane, $z(\vec{r})$ is the local surface roughness height, and Θ_B is the angle between the incident phonon momentum $\mathbf{q}$ and the ideally flat boundary surface normal. Note, $z(\vec{r})$ is employed as a normal random variable having $\langle z \rangle = 0$ and $\langle z^2 \rangle = \Delta^2$, where Δ is the rms surface roughness defined at the beginning of Section 2.2.3. Illustration reused here with permission from Ref. [3].

for boundary scattering depends on intrinsic scattering via a differential equation which gives rise to a scaling factor,

$$F_p(\boldsymbol{q}, H) = \frac{[1 - p(\boldsymbol{q})]\left(1 - exp\left[\frac{-H}{\tau_{j,int}(\boldsymbol{q})v_{j,\perp}(\boldsymbol{q})}\right]\right)}{1 - p(\boldsymbol{q})exp\left[\frac{-H}{\tau_{j,int}(\boldsymbol{q})v_{j,\perp}(\boldsymbol{q})}\right]} \,. \tag{2.9}$$

Here $\tau_{j,int}(\boldsymbol{q})^{-1}$ is the total scattering rate due to intrinsic mechanisms given in Eq. (2.3). The total scattering rate in the presence of both intrinsic and boundary interactions is the combination $\tau_j(\boldsymbol{q})^{-1} = \tau_{j,int}(\boldsymbol{q})^{-1} + \tau_{j,B}(\boldsymbol{q})^{-1}$. For a more complete derivation of the momentum-dependent specularity parameter, boundary scattering terms, and components to the steady-state pBTE in thin Si films and Si-Ge superlattices, we refer to earlier works by Aksamija and Knezevic [3, 7].

We can see in Eq. (2.8) that in thin films where the thickness H is less than the perpendicular component of the phonon mean free path (mfp) given by the product of the relaxation time due to intrinsic mechanisms $\tau_{j,int}(\boldsymbol{q})$ and the perpendicular component of the phonon group velocity vector $v_j^{\perp}(\boldsymbol{q})$, boundary roughness becomes the dominant scattering mechanism. The rate of boundary scattering depends strongly on the velocity perpendicular to the boundary. We can further analyze this dependence in the limiting case of completely diffuse boundaries (where specularity p =0) and weak intrinsic scattering. Then Eq. (2.8) reduces to a simpler form $\tau_{j,B}^{-1}(\boldsymbol{q}) = 2v_j^{\perp}(\boldsymbol{q})/H$, which is interpreted as saying that, in this limit where boundary scattering is dominant, phonon lifetime simply equals the average time it takes to reach a boundary. Then the rate of scattering due to boundary roughness is directly proportional to the component of the phonon group velocity in the direction perpendicular to the boundary. Consequently, decreases (increases) in velocity due to strain result in an increasing (decreasing) relaxation time, less (more) boundary scattering, and larger (smaller) thermal conductivity, respectively.

We anticipate the thermal conductivity in thin films to be more dependent on strain for this reason, especially the component of the thermal conductivity tensor (Eq. 2.1) in the CP direction perpendicular to the boundaries of the thin film. In this limit where boundary scattering is dominant over intrinsic, the diagonal components of the thermal conductivity tensor further simplify to

$$\boldsymbol{K}^{\parallel}(T) = k_B \frac{H}{2} \sum_j \sum_{\boldsymbol{q}} C_j(\boldsymbol{q}, T) \left[v_j^{\parallel}(\boldsymbol{q}) \right]^2 / v_j^{\perp}(\boldsymbol{q}) \tag{2.10}$$

for the IP (parallel to the film) direction and

$$\boldsymbol{K}^{\perp}(T) = k_B \frac{H}{2} \sum_j \sum_{\boldsymbol{q}} C_j(\boldsymbol{q}, T) v_j^{\perp}(\boldsymbol{q}) \tag{2.11}$$

for the CP (perpendicular to the film) direction. In this limit, we can see that the thermal conductivity is directly proportional to both the heat capacity and the corresponding component of the group velocity. Hence, we expect CP thermal conductivity to be highly sensitive to changes in phonon velocity caused by strain. The anisotropy between the IP and CP components of the tensor also increases in this limit approximately in proportion to the square of the ratio between the corresponding velocity components

$$\boldsymbol{K}^{\parallel}/\boldsymbol{K}^{\perp} \approx \sum_{j} \sum_{\boldsymbol{q}} \left[v_j^{\parallel}(\boldsymbol{q}) / v_j^{\perp}(\boldsymbol{q}) \right]^2 , \tag{2.12}$$

leading to a large potential anisotropy in thin films under biaxial strain.

In Fig. 2.3, we plot the energy-resolved longitudinal acoustic phonon velocity for the applied strains. In either Si or Ge, high-velocity LA phonons increase with compressive strain and decrease with tensile strain. Since biaxial strain produces asymmetry between the xy-plane and z-plane, we want to distinguish between transport in the direction of strain (in the xy-plane) and perpendicular to the direction of strain (the cross-plane or z direction). The inset in Fig. 2.3 represents the norm of the branch-wise velocity vectors for the three acoustic branches (one LA and two transverse TA1 and TA2). The solid lines represent the IP (parallel) direction, whereas the dotted lines represent the CP (perpendicular) direction. A clear decreasing trend is seen in the CP LA mode velocities from compressive strain to tensile strain with

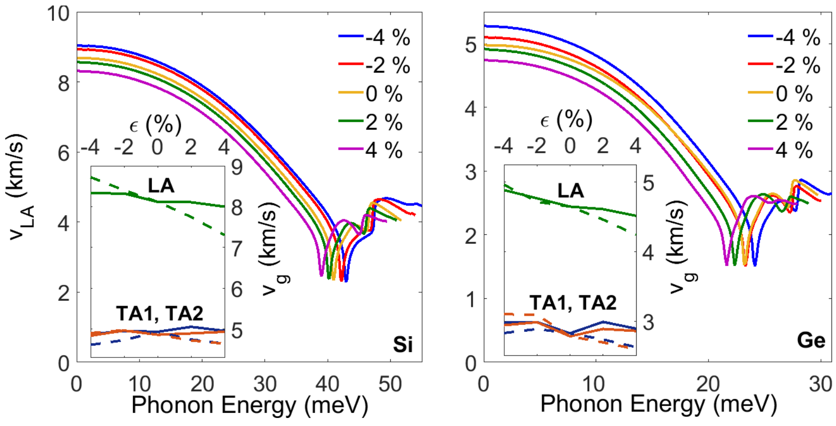

Figure 2.3. The energy-resolved velocities of the longitudinal acoustic (LA) mode shown for various strain amounts. The inset shows the three acoustic modes (TA1, TA2, and LA) transport/parallel (solid) and boundary/perpendicular (dashed) components of the group velocity vectors as a function of strain.

about 10% variation at the highest strains, while IP velocities show less variation. We do not plot the optical mode phonons here, because they generally have lower velocities and do not contribute greatly to heat transport in Si and Ge.

2.3 Calculation of IP and CP thermal conductivity

We have calculated the in-plane (κ_{IP}) and cross-plane (κ_{CP}) thermal conductivities of strained silicon and germanium thin-films from 1 to 500 K. A surface rms roughness height (Δ) of 0.45 nm is used as a typical value in calculating the boundary scattering with roughened surfaces. The corresponding lattice orientations for the IP and CP directions are [100] and [001] respectively. Due to lattice symmetry, the [100] direction and the [010] direction are virtually identical in the unstrained and biaxially strained materials. The thermal conductivities are presented in Fig. 2.4 where the IP conductivity is in good agreement with previous theoretical and experimental studies on silicon-on-insulator samples [3]. We note that, similar to previous studies on silicon, an anisotropy ($\kappa_{\mathrm{IP}}/\kappa_{\mathrm{CP}}$) of a factor of 2 is observed for the room-temperature IP and CP conductivity due to boundary scattering. We extend these observations to thin-films of germanium where a similar IP/CP anisotropy factor of approximately 1.8 is found.

The strain dependence for κ_{IP} is seen to be moderate for both Si and Ge. However, for κ_{CP} at temperatures above roughly 100 K compressive (tensile) strain can be seen to strongly increase (decrease) the overall conductivity. To better illustrate the strain dependence, the bottom panel in Fig. 2.4 shows the percent change in $\kappa_{\mathrm{IP,CP}}$ as a function of applied strain at room-temperature. We see a clear decreasing trend from a maximum boost of ~20% in Si (~25% in Ge) at 4% compressive strain to a decrease of ~15% in Si (~16% in Ge) in the CP conductivity at 4% tensile strain, while the IP conductivity remains relatively unchanged with variations <5% in Si (<10% in Ge) compared to the unstrained material. We note that our results are

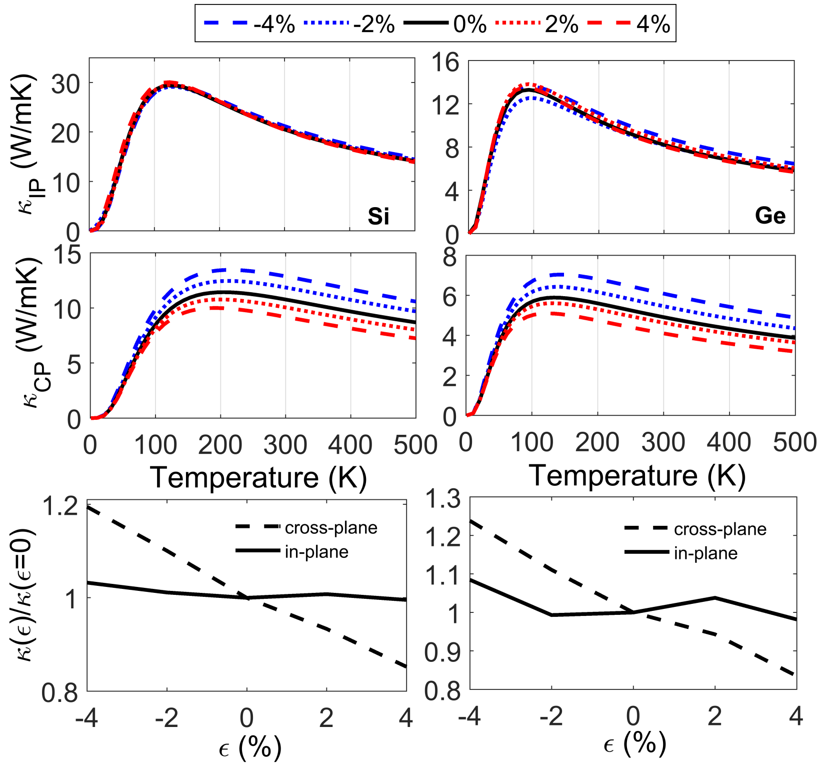

Figure 2.4. The in-plane (top) and cross-plane (middle) thermal conductivities for 20nm thick silicon (left) and germanium (right) thin-films with 0.45 nm surface roughness from 0 to 500 K. Strained materials are represented by blue (compressive) and red (tensile) dotted and dashed lines. (bottom) Change in thermal conductivity relative to the unstrained case as a function of strain for a 20 nm thin film with surface roughness 0.45 nm at 300K, showing significant strain dependence of cross-plane conductivity.

in agreement with prior theoretical [110] and experimental [73] studies supporting weak IP strain dependence and a stronger CP strain dependence. We can understand these trends based on Eqs. (2.10) and (2.11): the IP conductivity is driven more by phonons with large IP components of their group velocity. Such phonons interact less with boundary roughness, which is dependent on the CP velocity. In addition, heat capacity is also decreasing with tensile strain; taken together, tensile strain decreases heat capacity and IP velocity in the numerator of Eq. (2.10) but also decreases the CP velocity, hence resulting in less boundary scattering, and the two trends cancel.

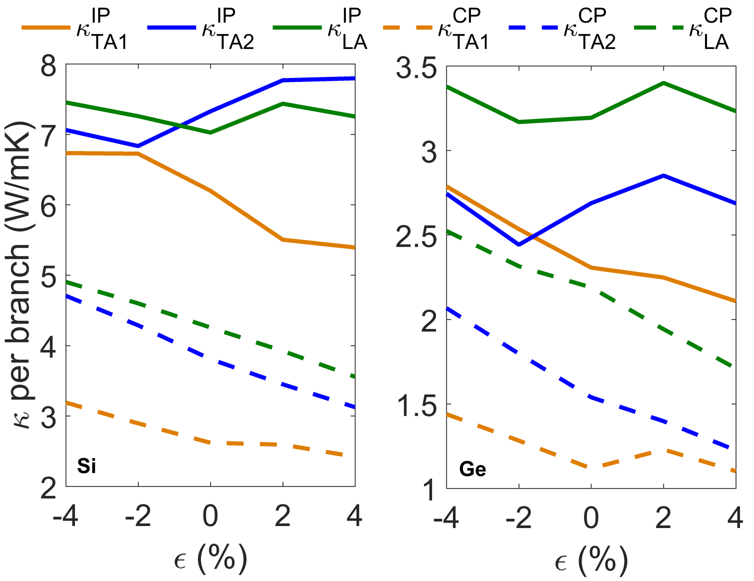

Figure 2.5. The branch-wise contribution to IP (solid lines) and CP (dash lines) thermal conductivities of the acoustic phonon modes at room temperature as functions of strain. While the IP TA2 and LA mode contributions show no definitive trend, the IP TA1 and all acoustic CP modes monotonically decrease from compressive to tensile strain.

In contrast, CP transport depends only on the CP component of phonon velocity (Eq. 2.11) so phonons having larger CP velocity (directed into the boundary) contribute more to the CP transport but they also encounter more boundary scattering. Hence, as tensile strain reduces both the CP velocity and heat capacity, the two trends add and result in a much more pronounced strain modulation than the IP conductivity. In Fig. 2.5 the room-temperature IP and CP conductivities presented in Fig. 2.4 are broken down into their acoustic mode contributions. Regarding the strain dependence of each acoustic mode, the TA2 and LA phonon modes for IP transport show no definitive trend, while the TA1 mode for IP and all acoustic modes for CP transport monotonically decrease from compressive to tensile strain. Collectively, for IP transport the variations due to strain in the acoustic mode contributions lead to very little change in the total conductivity. On the other hand, since all acoustic modes show similar strain dependence, their collective contribution to CP transport reveals a clear increase (decrease) with compressive (tensile) strain in the total conductivity.

2.4 Anisotropic transport as a function of film thickness

In addition, strain inherently promotes anisotropic transport by breaking lattice symmetry between the direction(s) of the applied strain and the direction(s) perpendicular to the applied strain direction. To further probe the effects strain has on the anisotropy between IP and CP transport, we have calculated the room-temperature thermal conductivity over several orders of magnitude of film thickness; the results are presented in Fig. 2.6. The right end of the horizontal axis represents a bulk like material where the left end represents thin-films with thickness approaching nanometer lengths. As expected, anisotropy in unstrained Si or Ge goes to one at the bulk limit.

As the thickness of the film becomes smaller and boundary roughness scattering begins to play a stronger role, we can see a clear increase in the anisotropy in the unstrained materials, in agreement with Eq. (2.12). The anisotropy between IP and CP thermal conductivity gradually increases with decreasing thickness reaching a peak value of 3 (~ 2.4) at 2 nm for unstrained Si (Ge) and that tensile (compressive) strain increases (decreases) this ratio at low thicknesses. As shown earlier in Fig. 2.4, only the CP conductivity shows a pronounced strain dependence; hence the anisotropy ratio $\kappa_{\mathrm{IP}}/\kappa_{\mathrm{CP}}$ shows an inverse relationship to κ_{CP}, increasing with tensile strains and decreasing for compressive strains.

We note that our model has been previously validated against experimental data on supported Si films down to 20 nm thickness [3]; below this value, phonon confinement effects may alter the phonon velocities [23], reducing thermal conductivity in the IP direction. The phonon confinement is counterbalanced by a reduction in the phase space available for scattering, which results in a reduced anharmonic phonon-

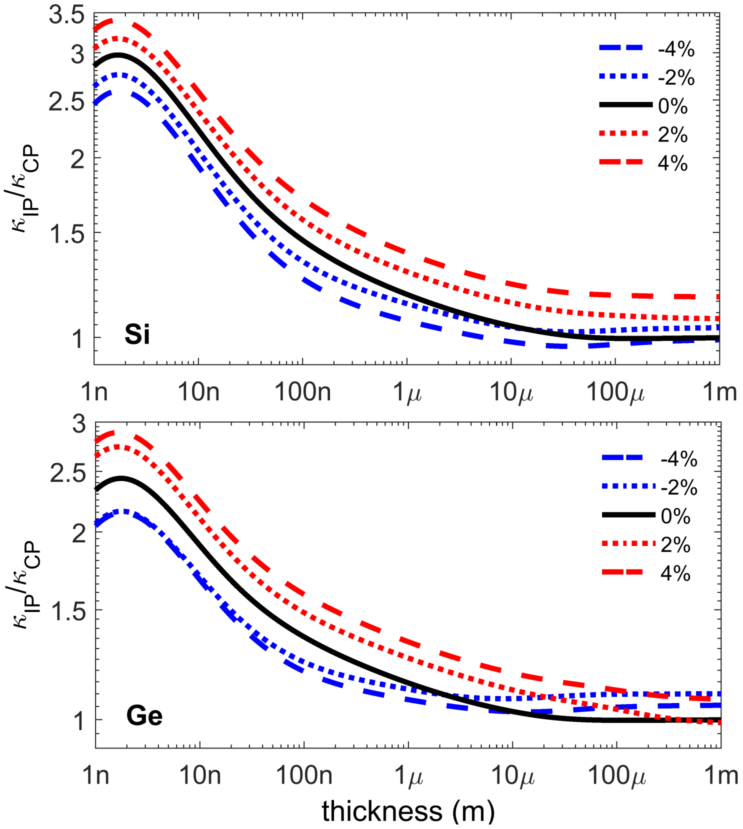

Figure 2.6. The ratio between room-temperature in-plane and cross-plane thermal conductivity as a function of film thickness. The unstrained case (black) converges to one as expected when the thickness approaches the mean-free-path of phonons. Compressive strain (blue) and tensile strain (red) cause anisotropy even at thickness comparable to the bulk phonon mean-free-path.

phonon scattering rates [22], so that the thermal conductivity of thin films below 13 nm is still dominated largely by boundary scattering and matches closely the predictions based on bulk lattice dynamics [105]. Prasher *et al.* [87] have shown that the heat capacity is also altered in ultrathin nanostructures (NWs) below a certain critical diameter. Based on the dominant phonon model, they relate this critical diameter to the dominant phonon wavelength [18, 19, 103], which is in the 1 to 10 nm range in Si [10, 42, 66]. Therefore, we consider the trends we observe in Fig. 2.6 below approximately 10-13 nm, including the peak in anisotropy at 2 nm, to be a qualitative indicator of the trends, while the strain dependence of the CP thermal conductivity holds across a broad range of thicknesses approximately up to the phonon mean-free-path, or so long as boundary scattering is dominant.

2.5 Chapter Summary

We have investigated the effects of biaxial strain on in-plane and cross-plane thermal transport in Si and Ge thin-films. We show that the anisotropy between in-plane and cross-plane thermal conductivities can be modulated with strain. This modulation is a result of velocity dependent boundary scattering which, in a strongly diffuse regime, depends roughly linearly on velocity. Our results indicate that strain may be an effective tool for modulating the cross-plane thermal conductivity in thin-films for efficient heat removal from strained Si/SOI and Ge/GOI devices.

CHAPTER 3

CROSS-DIMENSIONAL PHONON TRANSPORT IN A METAL-MONOLAYER-SUBSTRATE STACKS

In the previous chapter we revealed a unique strain dependence on cross-plane transport in Si and Ge thin-films due to the dominance of velocity dependent boundary scattering. As material/device downscaling is a traditional avenue for improved performance, let us continue the trend of decreasing film thickness – that is, in the limit of film thickness (H → single atom thickness) – and explore the role of boundaries/interfaces in atomic monolayers. The topic of boundaries with 2D materials often concerns itself with edge roughness at the monolayers (MLs) planar edge. Edge roughness in graphene has been extensively studied [31, 74, 30, 5, 6, 106], therefore we do not elaborate on it here. Instead we focus on the less explored topic of thermal transport across the interface formed between the monolayer and its underlying substrate. In this chapter, we will review a recently developed theoretical model for 2D-3D phonon transport and apply it to the case of encapsulated (3D-2D-3D stack) MLs. This model is general in that it can be applied to any 2D-3D vdW interface as long as the phonon density of states of each material is known. In addition, we will discuss the effects the substrate and (encapsulating) superstrate can have on the ML in a Ti-ML-SiO_2 (metal-ML-substrate) stacked system. We use first-principles DFPT simulations to obtain the phonon dispersion of our MLs (graphene and MoS_2) and the metal overlayer (Titanium). We show that an encapsulating layer can increase the thermal boundary conductance due to surface rayleigh waves in the superstrate which hybridize in the monolayer, and thus open an additional pathway for heat to transfer into the substrate. It is also evident that softer encapsulating layers, with low

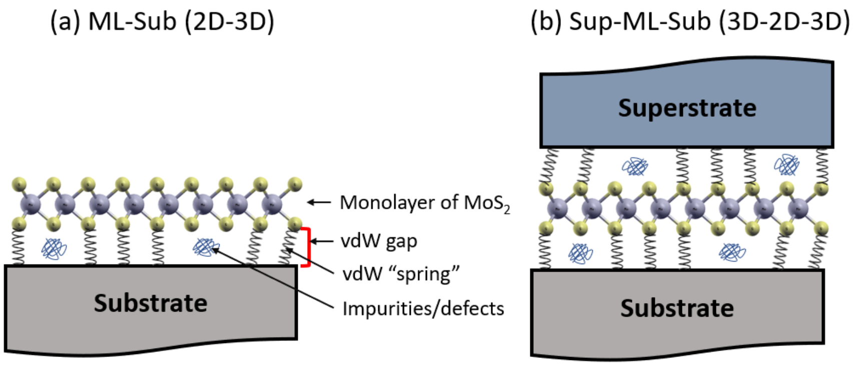

Figure 3.1. Schematic of the monolayer-substrate (a) and superstrate-monolayer-substrate (b) interface structures.

transverse sound velocities can improve TBC. Our model suggests that the thermal boundary conductance depends roughly quadratically on the spring coupling between the 2D-3D material. This work helps to emphasize the role of adhesion, which is related to the spring coupling, between the monolayer and substrate (or superstrate) as well as the choice of superstrate in influencing the overall cross-plane thermal boundary conductance (TBC) in a 3D-2D-3D stacked system.

3.1 Motivation

Since the first lab realization of atomic monolayers in 2004 [76, 75, 36], there has been a myriad of two-dimensional (2D) material discoveries [2, 50, 92, 11]. Atomically-thin 2D materials have promising potential for next-generation electronics and opto-electronics [111, 109], however heat dissipation from hot spots in the monolayer to its environment remains a critical concern to the design of 2D-based devices [116, 92, 107]. Thermal currents flowing in a monolayer (ML) can either dissipate through source/drain contacts, as in a transistor configuration, and/or through an often present supporting substrate via van der Walls interactions. When a monolayer is supported by a substrate, the interfacial area formed between the ML and substrate is often larger than the stacked (or lateral) source/drain contact interface area (or length). Thus it is suspected that the majority of waste heat dissipates across the ML-Sub interface and through the substrate [77]. For such reasons, it is imperative that the thermal boundary conductance (TBC) between MLs and substrates be well understood and boosted for reliable 2D-device lifetime and performance.

For bulk 3D-3D and same dimensional welded (convalently bonded) interfaces there exist two long-standing models for interfacial transport: the Diffuse Mismatch Model [96, 97] (DMM) and the Acoustic Mismatch model [62] (AMM). In the DMM, the interface is treated as completely diffuse where phonons impinging on the interface are destroyed and the probability of transmission or reflection is determined by the ratio of vibration density of states between the two materials. The DMM best models short-wavelength phonons that are perturbed by interface roughness features, however it often underestimates interfacial transport in cases where there is a large contribution from long-wavelength phonons due to smooth interface features between highly commensurate materials. For such smooth interfaces the AMM is often used, where phonon transport across the interface is determined by the acoustic impedances of either medium in a manner akin to Snell's Law. Interface transport models beyond these two methods bridge the gap between the DMM and AMM models by considering the specularity of incident phonons and better capturing the interplay between internal scattering, surface roughness, and acoustic mismatch between domains [7].

While most welded interfaces can be mapped between the limits given by the Acoustic and Diffuse Mistmatch Models, interfaces with van der Waals (vdW) gaps are not properly represented in these approaches. For such vdW interfaces, Prasher developed a variation of the AMM where a vdW coupling term is introduced [86]. In this approach the transmission coefficient is written in the following way,

$$\tau = \frac{4z_1 z_2 cos\theta_1 cos\theta_2}{(z_1 cos\theta_1 + z_2 cos\theta_2)^2 + \frac{\omega^2}{K_a^2}(z_1 z_2 cos\theta_1 cos\theta_2)^2} \ . \tag{3.1}$$

Here z_1 and z_2 are the acoustic impedances between either material, θ_1 and θ_2 are the angles between the interface normal and phonon propagation in either material, and K_a is the vdW spring coupling constant. In the limit of a welded interface where $K_a \to \infty$ the second term in the denominator vanishes, and we recover the AMM. On the other hand, when K_a is weak (large vdW gaps) the second term in the denominator dominates resulting in a quadratic dependence on spring coupling and phonon frequency $\tau \propto K_a^2/\omega^2$ – which suggests that low-frequency, long-wavelength phonons are primary TBC heat carriers in the limit of weak K_a.

The vdW+AMM model has been successfully been applied to 3D-3D interfaces involving a vdW gap [91]. However, in the case of 2D-3D interface transport, as in a monolayer-substrate system, the vdw-AMM cannot be used. The reasoning here is the following; in Eq. 3.1 the acoustic impedance of the ML $z_1 cos\theta_1 = \rho_1 v^{\perp}$ depends on the phonon velocity perpendicular to the interface. Since all ML phonons propagate in-plane and parallel to the interface, there are no phonon modes with non-zero $v^{\perp}$, hence the vdW+AMM gives a τ that is always 0. There are rare occasions where the vdW+AMM may work for 2D-2D interfaces as demonstrated in [113] where the authors investigated the thermal conduction properties of single and bundled boron nitride nanoribbons. However, it is important to note that the domains constructing the interface have the same phase space and that the $v^{\perp}$ is assumed to be some non-zero in-plane phonon velocity in order to insure on non-zero acoustic impedance. Thus, there is a need for a model for cross-dimensional 2D-3D interfaces beyond what has been previously discussed.

3.2 Methodology

In this section we will review a recently developed model for phonon transport across 2D-3D interfaces and discuss the approach for applying this model to a 3D-2D-3D stack. This model is general in that it can be applied to any 2D monolayer and 3D

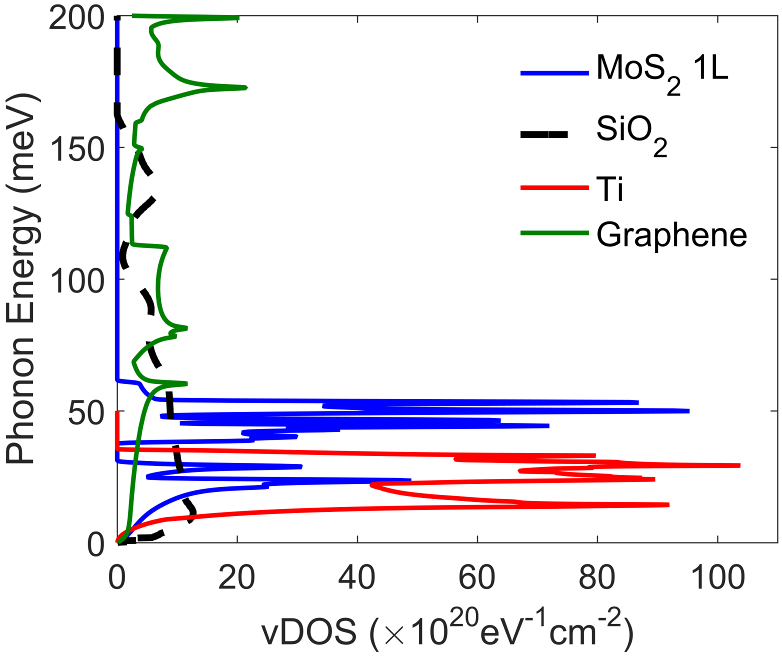

Figure 3.2. The phonon density of states of graphene, MoS$_2$, Ti, and SiO2. For graphene, MoS$_2$ and Ti the density of states was calculated from the full phonon dispersion obtained from first-principles DFPT simulations. The density of states of SiO$_2$ was extracted from [104].

material interface provided a vibrational density of states can be determined for both materials. We will apply this model to Ti-ML-SiO$_2$ systems where the ML will be either graphene or MoS$_2$. The phonon dispersions of graphene, MoS$_2$, and Titanium are calculated from first-principles simulations which are described in detail in the Appendix Sections A.1 and A.2. We then consider the effects the substrate and superstrate can have on the monolayer vibrational spectrum and how they influence the thermal boundary conductance in 3D-2D-3D stacked systems.

3.2.1 Review of 2D-3D Interface Transport Model

In previously discussed interface models (DMM, AMM, vdW+AMM), transport across the interface requires that phonons first collide with the interface. In the case of vdW bonded monolayer-substrate interfaces, phonons in the monolayer are always at the interface – thus, the depiction of phonons colliding with the interface is inaccurate and we must redefine the process that initiates interface transport. In a model developed in [21] phonon transfer across a 2D-3D interface is initiated when phonons in the monolayer are perturbed by substrate interactions or defects. This perturbation is caused by the coupling between monolayer atoms and surface atoms of the substrate having spring coupling constant K_a, as defined in Eq. 3.1, between them. In this perturbation phonons of mode $\boldsymbol{q}$ and branch j in the monolayer having frequency $\omega_j(\boldsymbol{q})$ hop across the interface transferring all of their energy $E = \hbar\omega_j(\boldsymbol{q})$ to the substrate where it ideally dissipates away from the monolayer.

A full derivation of the thermal boundary conductance is presented in [21]. In short, when a temperature difference $\Delta T = T_{ML} - T_{Sub}$ exists between the monolayer and substrate, the system is out-of-equilibrium, and there is a non-zero heat flux $Q(T)$ generated across the interface which can be written as an integral over the phonon spectrum as,

$$Q(T) = \int_0^\infty \hbar\omega \frac{dN^0(\omega,T)}{dT} \Delta T D_M(\omega)\Gamma_S(\omega) d\omega \; . \tag{3.2}$$

In the above, $D_M(\omega)$ is the monolayer vibrational density of states (vDOS), $\mathrm{d}N^0(\omega,T)/\mathrm{d}T$ is the temperature derivative of the Bose-Einstein distribution function for phonons $N^0(\omega,T) = [exp(\hbar\omega/k_BT) - 1]^{-1}$, and $\Gamma_S(\omega)$ is the substrate scattering rate that determines the rate at which phonons transfer across the interface. The thermal boundary conductance can then be calculated as the ratio between the net heat flux $Q(T)$ and the temperature difference ΔT as,

$$G(T) = \frac{Q(T)}{\Delta T} = \int C(\omega,T) D_M(\omega)\Gamma_S(\omega) d\omega \; , \tag{3.3}$$

where $C(\omega,T)$ is the modal heat capacity of the monolayer given as $C(\omega,T) = \hbar\omega\mathrm{d}N^0(\omega,T)/\mathrm{d}T$.

The substrate scattering rate Γ_S, which determines the rate at which phonons in the ML are perturbed by the substrate, was obtained from Perturbation Theory based on Fermi's golden rule performed by Seol *et al.* [93] Here we write Γ_S in the following way,

$$\Gamma_S(\omega) = \frac{\pi}{2} \frac{D_S(\omega)}{m_{ML} m_S} \frac{K_a^2}{\omega^2} \ , \tag{3.4}$$

where m_{ML} is the mass of the monolayer atoms in contact with surface atoms of the substrate with mass m_S, $D_S(\omega)$ is the vibrational density of states of the substrate taken in this chapter to be amorphous $\mathrm{SiO_2}$, ω is the phonon frequency, and K_a is the previously defined vdW spring coupling constant. From this equation, we can see that $\Gamma_S(\omega) \propto D_S(\omega) K_a^2/\omega^2$ which suggests that transmission across the interface, and therefore the thermal boundary conductance, increases quadratically with coupling strength and that long-wavelength, low-frequency modes contribute most to 2D-3D interfacial transport.

At this point it is important to note the phonon characters that contribute to interface transport in a 2D-3D system. It is quantitatively unclear how strongly each phonon mode (ZA, TA, LA) of the monolayer couples to the substrate, that is whether they couple equally each having $K_a = K_a^{ZA} = K_a^{TA} = K_a^{LA}$ or each have varying coupling strengths. In spite of this, one can explore various extreme cases by choosing values of spring coupling constants and comparing to experimental measurements. In fact, Seol et al. [93] performed such an investigation where it was shown that assuming $K_a^{TA} = K_a^{LA} = 0$ and $K_a^{ZA} > 0$ gave better predictions on in-plane transport when compared to experiments than when each acoustic branched coupled equally $K_a^{ZA} = K_a^{TA} = K_a^{LA}$. Additionally, in Correa *et al.* [21] we show that even if all three acoustic modes couple equally, the ZA mode of graphene still dominates in contribution.

This finding helps corroborate previous investigations on supported graphene which point to dampening of the ZA mode as the cause of reduced thermal conductivity – where an increase in dampening due to a substrate is indicative of strong coupling between the ZA mode and the substrate. For all intents and purposes, in this current chapter we assume $K_a^{TA} = K_a^{LA} = 0$ and that the ZA mode is the sole pathway of heat transport across a 2D-3D interface. This is important to note prior to the next two sections which will discuss how the supporting substrate and encapsulating layer of a 3D-2D-3D stack influence the monolayer dispersion and therefore the thermal boundary conductance.

3.2.2 Effects of a Supporting Substate on Monolayer Dispersion

When a monolayer is placed on a substrate, the atoms in the monolayer couple to the surface atoms in the substrate through weak van der Waals forces and hence transfer vibrational energy between them. Due to this coupling, long-wavelength flexural (ZA) phonons undergo a lifting in frequency caused by the collective interaction of the atomic vdW forces on long-wavelength modes [9, 98]. Starting from our full phonon dispersion of the monolayer, we modify the ZA mode to account for long-wavelength substrate interactions with the following equation, $\widetilde{\omega}_{ZA}(\mathbf{q}) = \sqrt{\omega_{ZA}^2(\mathbf{q}) + \omega_0^2}$; where ω_0 represents the amount of lifting. Subsequently the phonon velocities of near zone-center ZA modes are also modified – this is imposed by taking the gradient of $\widetilde{\omega}_{ZA}(\mathbf{q})$ with respect to $\mathbf{q}$. By applying the chain rule one can find that $\widetilde{v}_{ZA}(\mathbf{q}) = v_{ZA}(\mathbf{q})\omega_{ZA}(\mathbf{q})/\widetilde{\omega}_{ZA}(\mathbf{q})$. Since $\omega_{ZA}(\mathbf{q}) < \widetilde{\omega}_{ZA}(\mathbf{q})$ due to the lifting of the dispersion due to substrate interaction, the resulting phonon group velocities are always smaller than their counterparts in suspended monolayers.

In Fig. 3.3 we show the phonon dispersion of graphene (a) and MoS_2 (c) as calculated (dashed line) and after we impose the lifting to the ZA mode (red solid lines). The amount of offset ω_0 is calculated using the spring coupling constant K_a and the mass of the atoms in the monolayer m_{ML} that make contact with the substrate – precisely, $\omega_0 = \sqrt{K_a/m_{ML}}$ [84]. Note this is the same equation as the oscillating angular frequency of a simple harmonic oscillator. We can make such an assumption for the following reason: vdW forces are often modeled using a Lennard-Jones potential [86] which in the case of small displacements can be well-fit by the quadratic potential energy of a simple harmonic oscillator. Since phonon displacements are small – from fractions of an Å up to a few Å at most – we can safely make this assumption.

In Fig. 3.3b,d we show the vibrational Density of states (vDOS) before (dashed line) and after (solid line) the application of the long-wavelength offset for graphene

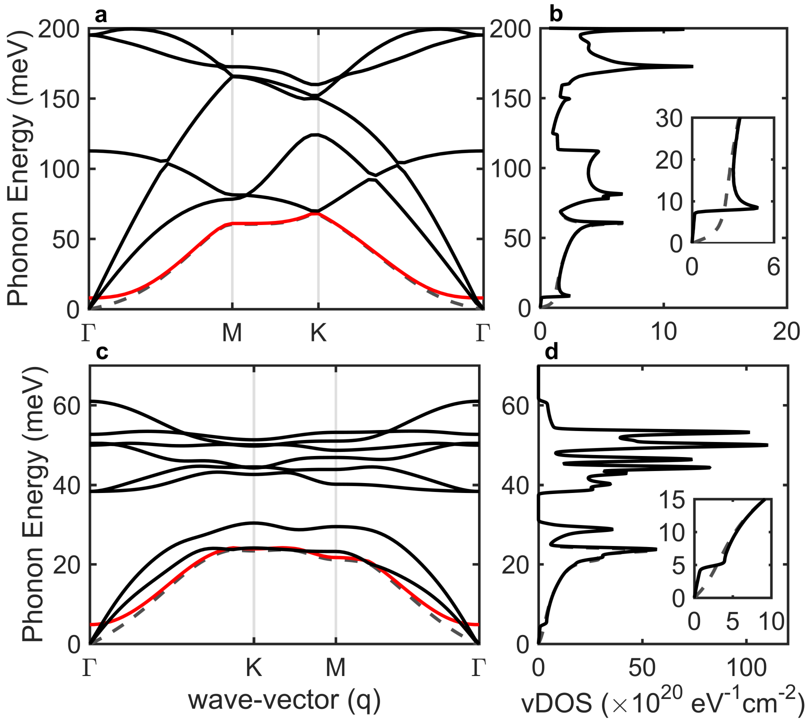

Figure 3.3. Shown here are the full phonon dispersions and vibrational density of states of graphene (a,b) and MoS_2 (c,d) after we apply the lifting in the ZA mode due to long-wavelength interactions with the substrate. The suspended (or as calculated) dispersion and DOS are shown by the dashed dark grey line whereas the gapped ZA mode is shown as a red solid line. The remaining phonon branches are shown as black solid lines. The insets in (b,d) show a close up of the resonant energy $\hbar\omega_0$ which is slight obscured in the full vDOS figures.

and MoS_2, respectively. Effectively, this offset is seen as a resonant peak in the vDOS that peaks at ω_0. Since the ZA mode is the only mode that contributes to cross-plane (2D-3D) transport (see end of Section 3.2.1), this means that there are no phonon modes in the monolayer beneath frequency ω_0 available to transfer heat into the substrate (or superstrate). Additionally, with respect to our substrate scattering rate this means that the energy range from 0 to (slightly below) $\hbar\omega_0$ does not contribute to heat transfer as it is negated by the zero DOS of the monolayer in that range; we say "slightly below" $\hbar\omega_0$ here simply because the phonon energy $\hbar\omega_0$ is roughly the onset of the ZA mode density of states.

3.2.3 Effects of an Encapsulating Layer

Common experimental techniques for measuring the thermal boundary conductance of thin-films and 2D materials such as the 3ω method [14, 20], ultra-fast laser-based thermoreflectance techniques [121, 15] and more recently electrical thermometry platforms [114] often involve depositing an metal layer on top of the ML-Sub (2D-3D, single-interface) stack essentially forming a 3D-2D-3D (double-interface) stack. Therefore, it is imperative to understand the physical effects an encapsulating layer can have on the monolayer and ultimately the thermal boundary conductance. In this section, we discuss the effects the encapsulating layer can have on the dispersion of the monolayer and interfacial transport.

Similar to the case of monolayer on substrate, when a monolayer is encapsulated by an overlayer (or superstrate) the surface atoms of the superstrate couple to the atoms in the monolayer through weak van der Waals forces. Consequently, an additional offset of long-wavelength flexural (ZA) mode phonons occurs that depends on the independent spring coupling constant between the superstrate and monolayer. For the remainder of this chapter we will refer to the spring coupling constant between ML-Sub and Superstrate-ML (Sup-ML) as K_{sub} and K_{sup}, respectively. In terms of the resonant frequency offset ω_0 (defined previously), we simply sum the spring coupling constants to arrive at $\omega_0 = \sqrt{(K_{sub} + K_{sup})/m_{ML}}$. Since weak van der Waals forces are forces of attraction, values of $K_{sub/sup}$ are always positive, and thus we always see an increase in the ZA mode offset ω_0 due to the presence of an encapsulating layer.

In addition to the increase in long-wavelength ZA-mode offset in the presence of the encapsulating layer, it has been found that Rayleigh waves of the superstrate hybridize with the monolayer and thus contribute to interfacial transport [77]. The Rayleigh waves are essentially surface waves that propagate on the surface of the superstrate due to collisions by transverse acoustic phonons in the superstrate with the boundary facing the Sup-ML interface. The Rayleigh wave modes (RWMs) have a linear dispersion given by the following equation $\omega_{\mathrm{RWM}} = c_{\mathrm{R}}||\mathbf{q}||$, where c_{R} is the sound velocity of the RWM which is close to the transverse acoustic sound velocity of the superstrate and $||\mathbf{q}||$ is simply the norm of the wave-vector $\mathbf{q}$.

The linear dispersion of the RWM closely resembles in-plane transverse and longitudinal acoustic modes of the monolayer in the long-wavelength regime, but with out-of-plane displacements much like the characteristic quadratic ZA mode of monolayers. In Fig. 3.4 we show the effective phonon dispersion and density of states of graphene (a,b) and MoS_2 (c,d) in the presence of both a supporting substrate and encapsulating layer. Here the encapsulating layer is taken to be titanium which has a transverse sound velocity of $c_{\mathrm{T}} = 3348$ m s^{-1}. Note this velocity is quite low as it is comparable to the sounds velocities of the softer acoustic modes of MoS_2 and noticably lower than the stiffer acoustic velocities of graphene. For this reason, we actually see a larger DOS contribution from the RWM in graphene than MoS_2 since there is already an appreciable presence of low-energy phonon modes in MoS_2 as compared to graphene.

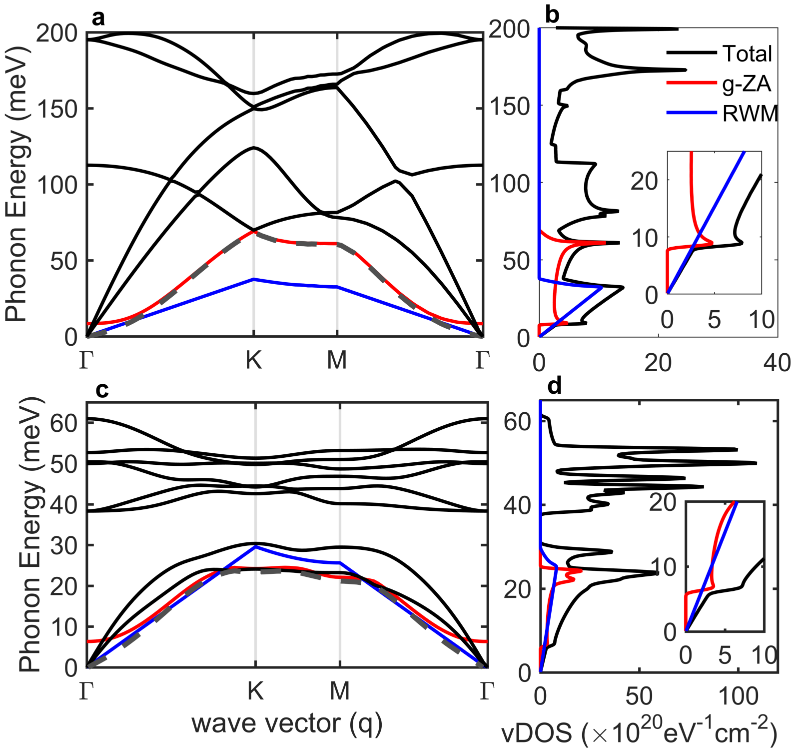

Figure 3.4. Full phonon dispersions of graphene (a) and MoS2 (c). The dashed grey line represents the ZA mode of suspended monolayers, and the solid red line represented the gapped ZA (g-ZA) mode characteristic of supported monolayers. The linear dispersion of the Rayleigh Wave mode is also represented here as the solid blue line. The remaining phonon modes are represented by the black solid lines. The vibrational density of states (vDOS) are depicted for graphene (b) and MoS2 (d). The insets show a low energy region where there is a resonant peak resulting from the spring coupling of the monolayer to the super- and substrate.

3.3 Results and Discussion

We will now apply the 2D-3D model to a 3D-2D-3D stacked system in light of the effects seen by the monolayer due to the presence of the substrate and superstrate described in the previous section. In doing so we will assume an amorphous SiO_2 substrate and a titanium encapsulating layer. We use relevant experimental data from [20, 57, 114] to help aid our calculations and discussion, but our predictions on TBC are not dependent on experimental measurements. Here it is important to note that in our model the spring coupling constant used in the offset of the ZA mode and the substrate scattering rate (Eq. 3.4) is treated as an input parameter. Therefore, we will fit our calculations to available experimental measurements by varying the spring coupling constant between the monolayer and relevant 3D material.

In Fig. 3.5a-d we show the low-energy phonon dispersion (a,b) and density of states (c,d) of graphene and MoS_2 (Gr,MoS_2). We emphasize the low-energy region here because the substrate scattering rate $\Gamma_{sub/sup}$ roughly follows a $D_S(\omega)K_a^2/\omega^2$ relationship, where the $1/\omega^2$ term indicates that long-wavelength, low-energy phonons contribute most to TBC. In 3.5a,b the grey dashed line represents the ZA mode of the suspended ML (as calculated from first-principles), the red solid line represents the gapped ZA (or g-ZA) mode which is lifted due to the simultaneous presence of the substrate and superstrate, and the blue line represents the RWM arising from the presence of the encapsulating layer (superstrate). The remaining solid black lines represent the in-plane TA and LA modes (as well as the optical modes) which do not contribute to interfacial transport – only the g-ZA and Rayleigh Wave modes contribute to interfacial transport.

In Fig. 3.5c,d we have the g-ZA mode and the RWM vDOS contributions shown as a red and blue solid line, respectively. The black solid line represents the vDOS of all phonon modes. The g-ZA mode leads to a resonant peak at $\hbar\omega_0$ due to the large contribution of long-wavelength modes caused by the flattening of the mode near zone-center. If we were to consider a ML-Sub interface alone only ZA phonons would contribute to TBC, and no phonon modes below $\hbar\omega_0$ would contribute. However, for the Sup-ML-Sub case, the emergence of the RWM provides phonon modes below $\hbar\omega_0$ that can contribute to interfacial transport. In addition, if we look at the ratio of the RWM contribution to the g-ZA mode contribution of both materials, the ratio is higher for graphene than for MoS_2. This is a direct consequence of the low-velocity of the RWM relative to the ZA mode velocities of graphene, whereas the softer MoS_2 monolayer has a lower ZA mode velocity and thus we see less of a difference in their vDOS contributions. This suggests that we should see a larger difference in the TBCs of graphene with and without the presence of the RWM as compared to $\mathrm{MoS_2}$.

In calculating the TBC of the Ti-ML-$\mathrm{SiO_2}$ stack we use the following procedure: $1^{\mathbf{st}}$) We replace the original ZA mode frequencies $\omega_{ZA}(\mathbf{q})$ with $\widetilde{\omega}_{ZA}(\mathbf{q}) = \sqrt{\omega_{ZA}^2(\mathbf{q}) + \omega_0^2}$ as in Section 3.2.2, but with $\omega_0 = \sqrt{(K_{sub} + K_{sup})/m_{ML}}$ as in Section 3.2.3. $2^{\mathbf{nd}}$) We add the hybridized RWM to the dispersion of the monolayer as a new branch having the dispersion $\omega_{\mathrm{RWM}} = c_{\mathrm{R}}||\mathbf{q}||$. $3^{\mathbf{rd}}$) We calculate the Sup-ML and ML-Sub scattering rates Γ_{sup} and Γ_{sub} based on Eq. 3.4 using their respective spring coupling constant terms and 3D material masses – that is, K_{sup} and the mass of Ti for Γ_{sup}, and K_{sub} and the average mass of $\mathrm{SiO_2}$ for Γ_{sup}. (Note it is the average

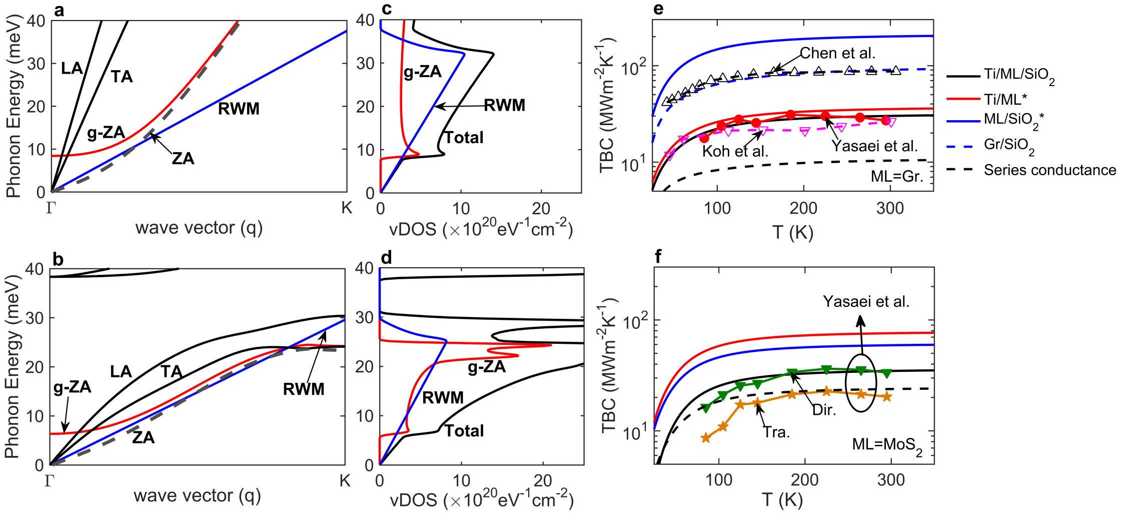

Figure 3.5. The low-energy region of the phonon dispersion of graphene (a) and MoS2 (b) where the gapped ZA (g-ZA) mode (solid red) is contrasted with the suspended ZA mode (dashed grey), and the linear Rayleigh Wave mode (solid blue) arising from encapsulation is shown. Similarly, the vibrational density of states for graphene and MoS2 are shown in (c) and (d), respectively. Thermal boundary conductance vs. temperature for single and double interfaces involving graphene (e) and MoS2 (f) from 25 to 350 K. The solid lines represent our theoretical results, while experimental data are represented by the lines with markers. The dashed black line is the series combination of two independent Ti/ML and ML/SiO2 single interfaces. The legend in the top right corner refers to data presented in figures (e) and (f) exclusively.

mass of SiO_2 only since the surface termination of SiO_2 is quantitatively unclear. That is, it is unclear if the surface terminates with more Si atoms, more O atoms or equal amounts – therefore we take the average for simplicity). $4^{\mathbf{th}}$**)** We take each $\Gamma_{sub/sup}$, compute $G_{sub/sup}(T)$ as in Eq. 3.3, and finally compute the total thermal boundary conductance as the sum of series conductances – Temperature dependent TBC $= G^{-1}_{total}(T) = G^{-1}_{sub}(T) + G^{-1}_{sup}(T)$.

In Fig. 3.5e,f we show the calculated TBC of Ti-ML-SiO_2 with ML being graphene in (e) and MoS_2 in (f). As we mentioned before, the values of $K_{sub/sup}$ are input parameters in our model. Therefore, starting in Fig. 3.5e we first use experimental data of a Gr/SiO_2 single-interface from Chen *et al.* [20] (black dashed line with upward facing triangles) to find a value of K_{sub} that gives the best fit (blue dashed line) on the measurement – this value turns out to be $K_{sub} = 2.25$ Nm^{-1}. From there keeping the same K_{sub}, we use experimental data from Koh *et al.* [57] (red solid line with red circles) and Yasaei *et al.* [114] (pink dashed line with downward facing triangles) for Ti-Gr-SiO_2 double-interfaces to find a value of K_{sup} that best fits (solid black line) their measurements – we get a $K_{sup} = 1$ Nm^{-1}.

Keeping $K_{sub} = 2.25$ Nm^{-1}, we then look at Ti-MoS_2-SiO_2 double-interfaces in Fig. 3.5f with provided experimental data from Yasaei *et al* [114]. Here we again vary K_{sup} to get a best fit (black solid line) on the direct-grown Ti-MoS_2-SiO_2 stack (green solid line with downward facing triangles) – this gives us a $K_{sup} = 2.7$ Nm^{-1}. The choice to keep K_{sub} fixed and vary K_{sup} is merely a means to an end, and it need-not be true that the spring coupling constant between Gr-SiO_2 and MoS_2-SiO_2 be the same. In fact, the adhesion between the Sup-ML and ML-Sub will depend on the ML, superstrate, substrate, and fabrication process used. For instance, we see an approximate 8-9 MWm^{-2}K^{-1} difference between direct-grown and transferred Ti-MoS_2-SiO_2 stacks. It is likely that the difference is attributed to the different fabrication approaches, leading to different adhesion energy (which is proportional to the spring coupling constant [21]) where the transferred MoS_2 on SiO_2 (orange line with stars) is surpassed by the direct-grown sample.

In both Fig. 3.5e,f the solid red and blue lines represent the extracted TBCs of the single-interfaces Ti-ML ($G_{sup}(T)$) and ML-SiO_2 ($G_{sub}(T)$) in the double-interface calculation. The sum of the series conductance of the red and blue solid lines recovers the black solid line for the whole Ti-ML-SiO_2 stack. The black dash line in either panel (e,f) represents the case if the two interfaces in the Ti-ML-SiO_2 stack are treated completely independent of each other. In that, we still have the same $K_{sub/sup}$ pairs, but we calculate the single-interface conductances $G_{sub/sup}$ with the individual ZA mode offsets from $K_{sub/sup}$ rather than their sum. In addition, in the black dashed line case since we treat the Ti-ML-SiO_2 stack as two independent 2D-3D interfaces, there is no RWM mode present.

This emphasizes the importance of treating the 3D-2D-3D stacked system as a whole rather than as two independent interfaces. Since an increase in the ω_0 offset alone (as a result of depositing an encapsulating layer) should lead to a decrease in TBC – due to the $1/\omega^2$ term in $\Gamma_{sub/sup}$ – we see the importance of the RWM contribution as we ultimately see an increase in TBC with the addition of the encapsulating layer. This states that the additional pathway for interfacial heat transport opened by the hybridized RWM more than offsets the increase in the ZA mode lifting caused by the encapsulating layer. Lastly, we see a much larger influence from the RWM in the Ti-Gr-SiO_2 stack than Ti-MoS_2-SiO_2 which corroborates our observation of the ratios of the vDOS between the RWM and the ZA mode earlier in this section.

Earlier we stated that our model is not dependent on experimental data, to show this we further study the role of K_a on the TBC by plotting the room-temperature TBC as a function of the vdW coupling K_a for graphene in Fig. 3.6a and MoS2 in Fig. 3.6b. The overall trend is nearly quadratic because the rate of phonon interaction with either substrate or superstrate metal $\Gamma_{sub/sup} \propto D(\omega)\ K_a^2/\omega^2$ is proportional to

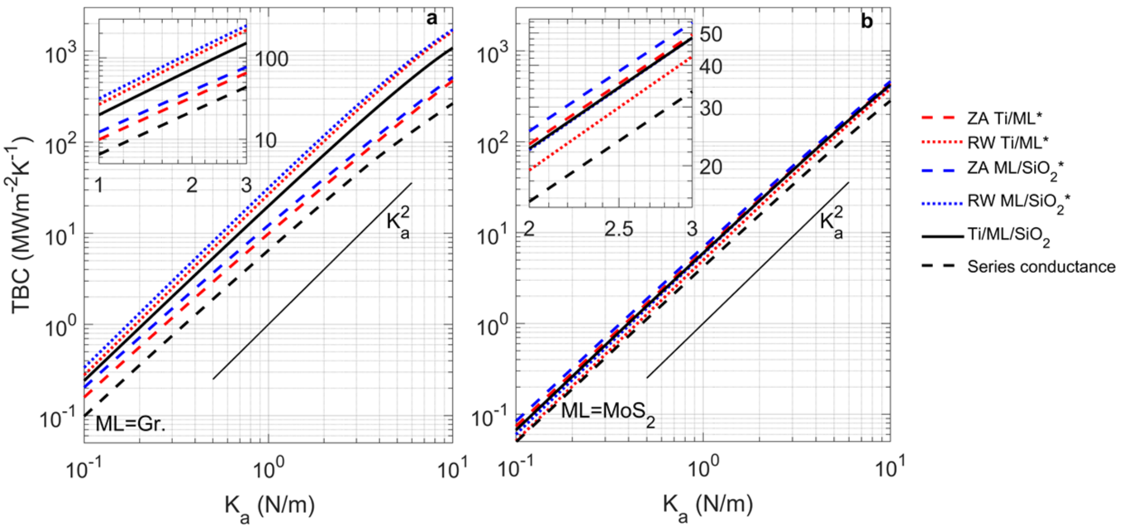

Figure 3.6. The dependence of room-temperature TBC on spring constant for single and double interfaces involving graphene (a) and MoS2 (b), respectively. Dashed red and blue lines are ZA, while dotted red and blue lines are the RWM contributions to each (Ti/ML and ML/SiO2) interface. Dashed black line is the series combination of two independent Ti/ML and ML/SiO2 single interfaces. The insets in (a) and (b) highlight the regions on the curves corresponding to the range of spring coupling constants used in the calculations in Fig. 3.5e and Fig. 3.5f above. Spring coupling constants in the range of [0.1, 10] N/m corresponds to a long-wavelength flexural mode offset range of [1.5, 14.7] meV for graphene and [0.9, 9] meV for MoS2.

the square of the coupling constant and inversely proportional to phonon frequency, suggesting that most of the heat being transferred is by long-wavelength modes. The solid black line represents the TBC of a Ti/ML/SiO2 stack where the long-wavelength ZA mode offset is $\omega_0 = \sqrt{2K_a/m_{ML}}$. The branch-wise breakdown per interface for the solid black line is shown by the color-coded dashed and dotted lines, where dashed (dotted) refers to the ZA (RWM) mode and red (blue) refers to the extracted TBC of the Ti/ML (ML/SiO2) interface. Note that in Fig. 3.6b for values of K_a >1 N/m the dotted blue line is under the solid black line. The dashed black line represents the TBC of a Ti/ML/SiO2 stack if the two interfaces (Ti-ML and ML-SiO2) were independent of one another. In other words, as if the presence of each interface has independent effects on the monolayer (i.e. $\omega_0 = \sqrt{K_a/m_{ML}}$) and no RWM is present. To show the trend in the K_a dependence of the TBC we also plot the curve TBC $= K_a^2$ in Figs. 3.6a,b which shows good agreement with both graphene and MoS_2. Ultimately the calculated TBC is slightly sub-quadratic in K_a, which is most pronounced in the ZA mode contributions to Ti/Gr* and Gr/SiO_2* at values of K_a >1-2 N/m of Fig. 3.6a.

3.4 Chapter Summary

We have reviewed a previously developed model for cross-dimensional 2D-3D phonon interface transport that is both computationally inexpensive and general for any monolayer-bulk interface provided that the vibrational density of states is known for both materials. We then take that model and apply it to 3D-2D-3D stacked systems and provide a discussion on the effects the substrate and superstrate can have on the monolayer dispersion and interfacial transport. We use the spring coupling constant (an approximation to the weak van der Waals forces) as an input variable to fit available experimental data. Our results show that the emergence of RWMs due to encapsulation offsets the increase in the ZA mode offset and leads to a doubling or tripling of the TBC. Our results also indicate that softer encapsulating layers with lower transverse sound velocity can boost the TBC, provided the spring coupling constant remains the same.

CHAPTER 4

EXTRINSIC EFFECTS ON PHONON TRANSPORT IN TRANSITION METAL DICHALCOGENIDE ALLOYS

So far we have investigated the unique strain dependence in cross-plane phonon transport due to velocity-dependent boundary scattering of phonons in quasi-two-dimensional Si and Ge thin-films down to several nanometers in thickness. Then we applied a 2D-3D cross-dimensional phonon transport model to calculate the thermal boundary conductance of 3D-2D-3D stacked systems based on graphene and MoS_2 monolayers. There, we outlined the effects of substrate and superstrate interactions on thermal boundary conductance (TBC), where it was shown that the TBC strongly depends on the spring coupling constant (K_a) at the interface and that the presence of an encapsulating superstrate can increase heat transfer from the monolayer to the substrate. In this chapter, we will take related aspects from Chapters 2 and 3, and apply them to transition metal dichalcogenide (TMD) ternary alloys; $MoS_{2-2x}Se_{2x}$, $WS_{2-2x}Se_{2x}$, $Mo_{1-x}W_xS_2$, and $Mo_{1-x}W_xSe_2$ for $x \in [0, 1]$. Alloying two materials together is a common engineering technique for tuning the electronic band gap and phonon frequencies between constituent materials, as well as introducing alloy scattering which greatly reduces thermal conductivity while minimally affecting electron transport [26, 59, 90, 53]. Here we investigate how alloying affects in-plane phonon transport in the presence of edge-roughness and a supporting SiO_2 substrate, as well as alloying effects on the TBC between TMD alloys and SiO_2. Our results show that through alloying alone, the lattice thermal conductivity can be significantly reduced even at modest alloying compositions. Further, with the introduction of (extrinsic) atomically rough edges through nanostructuring and substrate effects the thermal conductivity drops by at least another factor of 3 or more. We also show that alloy composition dependence of TBC is modest and qualitatively different than in-plane transport. Our results show that through the combination of alloying and extrinsic effects one can modulate the in-plane thermal conductivity and through-plane (TBC) conductance of TMD alloys. The former being beneficial for thermoelectric applications which require ultra-low thermal conductivity, and the latter would help improve waste heat removal from hot-spots in the active-layer of 2D-based devices.

4.1 Overview of thermal transport in 2D TMDs

The thermal transport properties of transition metal dichalcogenide (TMDs) has been studied both theoretically [39, 80, 44, 120] and experimentally [112, 79, 118, 51]. Early experimental measurements of the in-plane thermal conductivity κ_{IP} via raman spectroscopy of single-layer suspended $\mathrm{MoS_2}$ [112] and $\mathrm{WS_2}$ [79] show rather low values of 34 and 32 $\mathrm{W.m^{-1}.K^{-1}}$, respectively. These measurements contradicted available theoretical predictions for single-layer suspended $\mathrm{MoS_2}$ and $\mathrm{WS_2}$ from calculations, that combined density functional theory (DFT) and a Peierls-Boltzmann transport (PBTE) model, which placed the in-plane thermal conductivities of $\mathrm{MoS_2}$ and $\mathrm{WS_2}$ at 103 and 142 $\mathrm{W.m^{-1}.K^{-1}}$ [39], respectively. Later, a DFT-driven Slack model for the thermal conductivity predicted low κ_{IP} values ($\sim 30-33$ $\mathrm{W.m^{-1}.K^{-1}}$) [80] for $\mathrm{MoS_2}$ and $\mathrm{WS_2}$ in agreement with the measured values from [112, 79]. However, raman spectroscopy performed in [118] demonstrates κ_{IP} of $\mathrm{MoS_2}$ and $\mathrm{MoSe_2}$ as high as 84 ± 17 and 59 ± 18, respectively, which surpass the lower measurements in [112, 79] and are in good agreement with DFT+PBTE [39]. More recent theoretical calculations provide further support for $\kappa_{\mathrm{IP}} > 70$ $\mathrm{W.m^{-1}.K^{-1}}$ for sulfides ($\mathrm{MoS_2}$ and $\mathrm{WS_2}$) and $\kappa_{\mathrm{IP}} \approx 50\pm10$ $\mathrm{W.m^{-1}.K^{-1}}$ for selenides ($\mathrm{MoSe_2}$ and $\mathrm{WSe_2}$). Non-equilibrium molecular dynamics and Green-Kubo method were employed [44] to calculate κ_{IP} in the zig-zag and armchair directions. There, the authors report for single-layer $\mathrm{MoS_2}$ $\kappa_{\mathrm{IP}}^{zigzag} = 110$

W.m^{-1}.K^{-1} and $\kappa_{\mathrm{IP}}^{armchair} = 100$ W.m^{-1}.K^{-1}, and for MoSe$_2$ $\kappa_{\mathrm{IP}}^{zigzag} = 44$ W.m^{-1}.K^{-1} and $\kappa_{\mathrm{IP}}^{armchair} = 41$ W.m^{-1}.K^{-1}. This was followed by DFT-driven phonon Boltzmann transport equation (pBTE) predictions [120] of 82.2, 121.2, 46.2, and 72.7 W.m^{-1}.K^{-1} for MoS$_2$, WS$_2$, MoSe$_2$, and WSe$_2$ respectively. These theoretical predictions are then followed by time-domain thermoreflectance (TDTR) measurements [51] of κ_{IP} on bulk, natural TMDs (MoS$_2$, WS$_2$, MoSe$_2$, and WSe$_2$). In-plane conductivity values obtained from TDTR were 82, 120, 35, and 42 W.m^{-1}.K^{-1} for MoS$_2$, WS$_2$, MoSe$_2$, and WSe$_2$ respectively. Although the values from TDTR are on bulk multilayer TMDs, the in-plane conductivity values serve as a baseline for comparison to single- and few-layer suspended TMDs [51].

There has been far less attention given to the thermal properties of TMD alloys, despite their potential applications in solid-state memory and thermoelectric devices [40, 61]. The in-plane thermal conductivity of a Mo$_{1-x}$W$_x$S$_2$ alloy with and without WSe$_2$ nanoclustering was investigated via DFT+PBTE [40]. DFT+PBTE revealed a minimum of ∼20 W.m^{-1}.K^{-1} at ∼40% W mixing, only reduced further by ∼10% through the introduction of nanoclustering. The thermal properties of janus[1] MoSSe was investigated [41] with a DFT+pBTE model where a room-temperature value for the compound was found to be 14.9 W.m^{-1}.K^{-1}. Very recently, anisotropic thermal transport (in-plane and cross-plane) was studied [88] in layered 2H- and Td-phase WSe$_{2(1-x)}$Te$_{2x}$ alloys using a combination of TDTR measurements and DFT calculations. There, the minimum κ_{IP} for 2H-phase alloys was ∼10 W.m^{-1}.K^{-1}. Despite these works, there is still a lack of investigations into the thermal conductivities of suspended and supported single-layer ternary TMD alloys. In this work we use a DFT-driven pBTE model to study boundary effects on homogeneous and ternary

---

[1] *Janus* transition metal dichalcogenides are compound materials and represent a class of TMDs where one of the layers of chalcogen atoms are completely replaced by a different chalcogen species [117]. For example, janus MoSSe is the compound S-Mo-Se with no randomization between chalcogen species.

TMD alloy nanoribbons as well as the alloy composition dependence of κ_{IP} of suspended and supported TMDs. We also use our 2D-3D interface model to study the thermal boundary conductance dependence on alloy mixing of SiO_2 supported TMD alloys.

4.2 Methodology

We start by calculating the full phonon dispersion of four TMDs of the type MX_2, where M=Mo,W and X=S,Se, from first-principles density functional perturbation theory (DFPT) simulations. The resulting full phonon dispersions of the four homogeneous TMDs are plotted in Fig. 4.1 (simulations discussed in Appendix A.3). We then approximate a virtual alloy dispersion using a *virtual crystal approximation* (de-

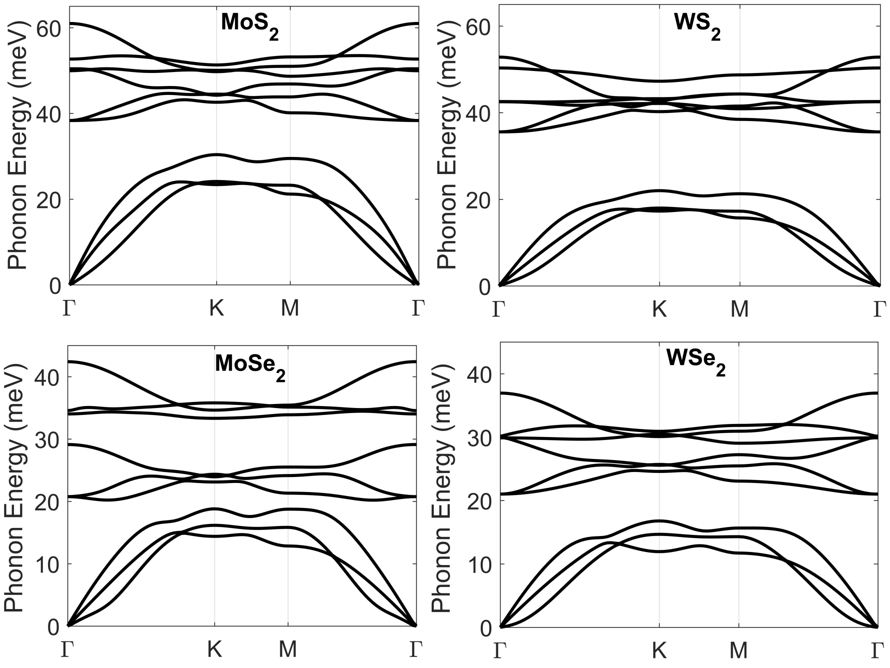

Figure 4.1. The full phonon dispersion is shown for MX_2 TMDs where M=Mo, W and X=S, Se. Starting from MoS_2, the phonons energies decrease as W and Se atoms replace Mo and S, respectively. The reduction is primarily driven by the increased unit cell mass and larger lattice constants from the heavier W and Se atoms (See Table 4.1).

tailed in the next Section) and use it as input data to a phonon Boltzmann transport equation (pBTE). Our pBTE model for two-dimensional thermal conductivity follows Allen's modified Callaway model [65] and takes into consideration all relevant scattering mechanisms; three-phonon normal and umklapp, isotope, alloy mass-difference, line-edge roughness, and substrate scattering. We then use our 2D-3D phonon transport model to investigate the TBC between TMD alloys on SiO_2.

4.2.1 Virtual Crystal Approximation

In the *virtual crystal approximation* (VCA), material properties of two or more materials are mixed, often linearly, to arrive at approximated material properties for a virtually alloyed material. The simplicity of the VCA is attractive for its computational cost but limiting in its accuracy of representing practical alloys whose inherent randomness breaks long-range periodicity, which the VCA preserves. Therefore, the VCA is generally coupled with an additional scattering mechanism, termed alloy (mass-difference or mass-disorder) scattering, to account for additional anharmonicty caused by the disordered mixing of masses between the alloyed species [58]. Traditionally, the VCA has been successful in predicting the material properties of alloyed Group IV semiconductors and Group III-V Nitrides [33, 35, 63]. Here we use the VCA to mix the lattice constants, atomic mass, phonon dispersion, and group velocities of 2D single-layer TMDs.

In implementing the VCA here we follow a similar approach as the one detailed in [53] where one can write the alloyed materials' unit cell mass and lattice constant as a linear combination of the constituent materials, as $m_{alloy} = (1-x)m_1 + xm_2$ and $a_{alloy} = (1-x)a_1 + xa_2$. Unit cell masses and lattice constants for the four homogeneous TMDs used in this work are shown in Table 4.1. Next, we compute the phonon dispersion and group velocities of the alloy from the corresponding values of the homogeneous materials as,

Table 4.1. Unit cell masses (m) and lattice constants (a_0) for homogeneous TMDs. The unit cell masses are obtained through simple summation of the three atom basis of MX_2 TMDs, as in $m = m_{\mathrm{M}} + 2m_{\mathrm{X}}$. The lattice constants for WS_2, $MoSe_2$ and WSe_2 represent the equilibrium structure parameters achieved after structural relaxation where the forces on each atom are $< 5 \times 10^{-4}$ eV/Å (See Appendix A.3).

	MoS_2	WS_2	$MoSe_2$	WSe_2
m (a.u.)	160.06	247.96	253.86	341.76
a_0 (Å)	3.165†	3.19	3.288	3.321

$$\omega_{alloy}(\mathbf{q}, j) = \left[\frac{(1-x)m_1 a_1^2 \omega_1^2(\mathbf{q}, j) + x m_2 a_2^2 \omega_2^2(\mathbf{q}, j)}{m_{alloy} a_{alloy}^2} \right]^{1/2} , \tag{4.1}$$

and

$$\vec{v}_{alloy}(\mathbf{q}, j) = \frac{(1-x)m_1 a_1^2 \omega_1(\mathbf{q}, j) \vec{v}_1(\mathbf{q}, j) + x m_2 a_2^2 \omega_2(\mathbf{q}, j) \vec{v}_2(\mathbf{q}, j)}{m_{alloy} a_{alloy}^2 \omega_{alloy}(\mathbf{q}, j)} . \tag{4.2}$$

In Fig. 4.2 we plot the phonon dispersion of MoS_2, WS_2, and a 50% (x=0.5) mixed $Mo_{1-x}W_xS_2$ alloy. As tungsten (W) atoms are introduced the phonon dispersion decreases, interpolating between the dispersions of the homogeneous materials. The VCA has been used previously in [40] to study phonon transport in single-layer $Mo_{1-x}W_xS_2$ alloys embedded with WS_2 nanodomains. There, the VCA was applied more rigorously at the level of interatomic force constants which were then used to extract phonons frequencies, whereas here we have applied VCA in the latter stage at the level of the phonon frequencies themselves. Despite this fact, we find that the acoustic modes, the primary heat carriers, agree well with the alloyed phonon dispersion presented in [40].

[†] The lattice constant for MoS_2 is chosen from structural relaxations performed using a GGA functional which are known to better reproduce experimental measurements [80], whereas in our DFPT simulations an LDA functional was implemented for MoS_2 (See Appendix A.1) which tends to underestimate the lattice constant [16].

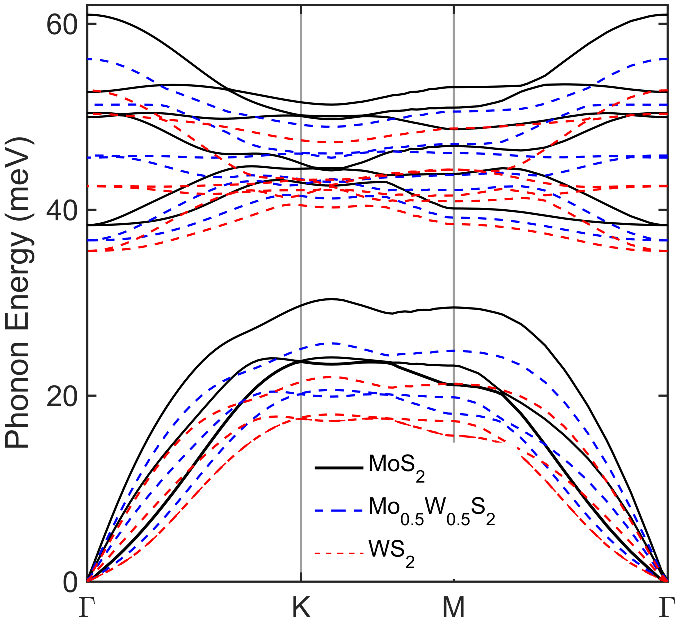

Figure 4.2. The full phonon dispersion of MoS$_2$ (black solid), WS$_2$ (red dash), and Mo$_{0.5}$W$_{0.5}$S$_2$ (blue dash). Through the introduction of W atoms, we see a gradual reduction in the phonon spectrum that interpolates between the dispersions of the homogeneous materials.

4.2.2 In-plane Phonon Transport

The phonon Boltzmann transport equation (pBTE) has been used to study thermal transport in semiconductor materials [34, 53] as well as two-dimension graphene [65]. Here we use Allen's solution [8] to the pBTE, which is a slight modification to Callaway's original model [17]. Normal scattering processes are non-resistive because they conserve crystal momentum and thus do not inhibit thermal transport but rather lead to a redistribution of phonon modes [17]. Both Callaway and Allen sought to correct the underrepresentation of non-resistive normal phonon scattering to the thermal conductivity. In either approach the steady-state pBTE is written as,

$$\vec{v}(\mathrm{q}, j) \cdot \nabla_{\vec{r}} N_{\mathbf{q}} = -\frac{N_{\mathbf{q}} - N_{\mathbf{q}}^0}{\tau_R(\mathbf{q}, j)} - \frac{N_{\mathbf{q}} - N_{\mathbf{q}}^*}{\tau_N(\mathbf{q}, j)} \ , \tag{4.3}$$

where on the left hand side $\vec{v}(\mathrm{q}, j)$ is the phonon velocity and $\nabla_{\vec{r}} N_{\mathbf{q}}$ is the spatial gradient of the out-of-equilibrium distribution function $N_{\mathbf{q}}$. While on the right hand side, $\tau_R^{-1}(\mathbf{q}, j)$ represents the resistive scattering rate which relaxes the out-of-equilibrium distribution back to a zero heat flux equilibrium distribution $N_{\mathbf{q}}^0$, represented by the Bose-Einstein distribution function $N_{\mathbf{q}}^0(T) = [\exp(\hbar\omega(\mathbf{q})/k_B T) - 1]^{-1}$, and $\tau_N^{-1}(\mathbf{q}, j)$ represents the non-resistive (normal) scattering rate that pushes the out-of-equilibrium distribution toward a non-zero heat flux flowing equilibrium distribution $N_{\mathbf{q}}^*$.

In solving for the thermal conductivity κ, both Allen and Callaway models arrive at the general form,

$$\kappa = \kappa_{\mathrm{RTA}} + \frac{\lambda_1 \lambda_2}{\lambda_3} \ , \tag{4.4}$$

which consists of the widely used relaxation time approximation (RTA) term κ_{RTA} plus a correction term $\frac{\lambda_1 \lambda_2}{\lambda_3}$. The RTA term is written as

$$\kappa_{RTA}^{\alpha\beta}(T) = \frac{k_B}{h_{2D}} \sum_j \sum_{\mathbf{q}} \hbar\omega(\mathbf{q}, j) \frac{\partial N_0(T)}{\partial T} \tau_C(\mathbf{q}, j) v^{\alpha}(\mathbf{q}, j) v^{\beta}(\mathbf{q}, j) \ , \tag{4.5}$$

where k_B is Boltzmann's constant, h_{2D} is the 2D layer thickness (including interplanar vdW gap), $\hbar\omega(\mathbf{q}, j)$ represents phonon energy, $\frac{\partial N_0(T)}{\partial T}$ is the temperature derivative of the equilibrium Bose-Einstein distribution function, $\tau_C(\mathbf{q}, j)$ is the total relaxation time, and $v^{\alpha,\beta}(\mathbf{q}, j)$ represents the phonon group velocity in the α and β cartesian directions. In Allen's solution $\lambda_{1,2,3}$ are written in the following form,

$$\lambda_{1,j} = \frac{1}{A\delta} \sum_{\mathbf{q}} v_{\parallel}(\mathbf{q}, j) q_{\parallel} \tau_C(\mathbf{q}, j) \frac{\partial N_{\mathbf{q}}}{\partial T} \ , \tag{4.6}$$

$$\lambda_{2,j} = \frac{1}{A\delta} \sum_{\mathbf{q}} v_{\parallel}(\mathbf{q}, j) q_{\parallel} \left[\frac{\tau_C(\mathbf{q}, j)}{\tau_N(\mathbf{q}, j)} \right] \frac{\partial N_{\mathbf{q}}}{\partial T} \ , \tag{4.7}$$

$$\lambda_{3,j} = \frac{1}{A\delta}\sum_{\mathbf{q}}\left(\frac{q_{\|}^2}{\hbar\omega_{\mathbf{q},j}}\right)\left[\frac{\tau_C(\mathbf{q},j)}{\tau_R(\mathbf{q},j)}\right]\frac{\partial N_{\mathbf{q}}}{\partial T} \ , \tag{4.8}$$

where $q_{\|}$ is the component of the phonon wave-vector that is perpendicular to the boundary normal. Collectively, $\lambda_{1,2,3}$ quantify the additional thermal conductivity produced by the flowing equilibrium. In Eqs. (4.5-4.8), $\tau_C(\mathbf{q},j)$ combines all resistive $\tau_R(\mathbf{q},j)$ and non-resistive $\tau_N(\mathbf{q},j)$ scattering mechanisms, that is $\tau_C^{-1}(\mathbf{q},j) = \tau_R^{-1}(\mathbf{q},j) + \tau_N^{-1}(\mathbf{q},j)$.

The anharmonic phonon-phonon normal scattering rate used here follows the work of Morelli *et al.* [72] where $\tau_N^{-1}(\mathbf{q},j) = B_N\omega_{\mathbf{q},j}^{a_N}T^{b_N}e^{-\Theta_j/3T}$ and

$$B_N(a_N,b_N) = \left(\frac{k_B}{\hbar}\right)^{b_N}\frac{\hbar\gamma_j^2[S_0h_{2D}]^{(a_n+b_N-2)/3}}{\overline{M}v_j^{a_N+b_N}} \ . \tag{4.9}$$

In the above, Θ_j is the branch-wise debye temperature, γ_j is the branch-wise Grüneisen parameter, S_0 is the surface area of the 2D layer unit cell ($S_0 = \frac{\sqrt{3}}{2}a_0$ for homogeneous TMDs or $S_0 = \frac{\sqrt{3}}{2}a_{alloy}$ for alloyed TMDs), and $\overline{M}$ is the unit cell atomic mass (i.e., values in Table 4.1 for homogeneous TMDs or values from m_{alloy} defined in Sec. 4.2.1 for alloyed TMDs). The emprical exponential factors a_N and b_N that determine the frequency and temperature dependencies are $[1\ 2\ 2]_j$ and 1, respectively. The Grüneisen parameter, which determines the anharmonicity of phonon-phonon interactions (where larger values represent more anharmonicity) [80], is 2 for all branches.

Resistive scattering mechanisms are comprised of any collision that destroys crystal momentum, which includes anharmonic umklapp scattering $\tau_U^{-1}(\mathbf{q},j)$, isotope scattering $\tau_{iso}^{-1}(\mathbf{q},j)$, impurity scattering $\tau_{imp}^{-1}(\mathbf{q},j)$, alloy mass-difference scattering $\tau_{mass}^{-1}(\mathbf{q},j)$, line-edge roughness scattering $\tau_{LER}^{-1}(\mathbf{q},j)$, and substrate scattering $\tau_{sub}^{-1}(\mathbf{q},j)$. The scattering rate of resistive processes is thus written as

$$\begin{aligned}\tau_R^{-1}(\mathbf{q},j) &= \tau_U^{-1}(\mathbf{q},j) + \tau_{iso}^{-1}(\mathbf{q},j) + \tau_{imp}^{-1}(\mathbf{q},j) + ...\\ &\quad ... + \tau_{mass}^{-1}(\mathbf{q},j) + \tau_{LER}^{-1}(\mathbf{q},j) + \tau_{sub}^{-1}(\mathbf{q},j) \ . \end{aligned} \tag{4.10}$$

We again follow the work of [72] in considering anharmonic umklapp processes as, $\tau_U^{-1}(\mathbf{q}, j) = B_U \omega_{\mathbf{q},j}^{a_U} T^{b_U} e^{-\Theta_j/3T}$ where

$$B_U(a_U, b_U) = \frac{\hbar \gamma_j^2}{\overline{M} v_j^{a_U} \Theta_j^{b_U}} \ . \tag{4.11}$$

Here the values of a_U and b_U are 2 and 1, respectively. Normal and umklapp scattering typically dominate in bulk crystals where sample dimensions are large and impurities/defects are low in concentration, however here we are interested in studying phonons in the presence of boundaries of alloyed materials. Hence, strong boundary scattering from nanostructuring and mass-difference scattering from alloying will dominate over three-phonon (N and U) processes and determine the effective relaxation time of phonons. The remaining scattering mechanisms can be grouped as mass-disorder scattering (τ_{iso}^{-1}, τ_{imp}^{-1}, and τ_{mass}^{-1}) and extrinsic boundary/interface scattering (τ_{LER}^{-1} and τ_{sub}^{-1}).

Phonon scattering due to mass-disorder can occur with isotopes, vacancies/impurities, and atoms with different atomic mass than the host species (e.g., in alloys). These mechanisms are elastic and can be written independent of the phonon wave-vector ($\mathbf{q}$) as [100, 99],

$$\tau_{iso}^{-1}(\omega) = \frac{\pi S_0}{12} \Gamma_{iso} \omega^2 D_{2D}(\omega) \ , \tag{4.12}$$

where Γ_{iso} is the natural abundance of isotopes $\Gamma_{iso} = \chi(1-\chi)/(\overline{M}+\chi)^2$ with $\chi =$ 3.4%. The phonon density of states $D_{2D}(\omega)$ is calculated following the Brillouin zone integration method [38], which for dense q-point grids can be numerically calculated as a sum over all phonon modes $\mathbf{q}$ and branches j, $D_{2D}(\omega) = \sum_{\mathbf{q},j} \delta[\omega - \omega(\mathbf{q}, j)]$. Scattering with impurities occurs with lattice vacancies/defects and are calculated as,

$$\tau_{imp}^{-1}(\omega) = \frac{\pi S_0^2}{12} n_{imp} \omega^2 D_{2D}(\omega) \ , \tag{4.13}$$

where n_{imp} represents the concentration of impurities. Typically, the mass-difference of isotopes is small and when abundance is low, phonon-isotope scattering is weak. Similarly, phonon-impurity scattering depends largely on its concentration and does not contribute largely to the effective relaxation time until n_{imp} is comparable to the atomic density of the host material. In this work, we consider the abundance of isotopes and impurities to be small and hence they do not contribute greatly to τ_R^{-1}. On the other hand, scattering caused by the mass-difference in alloys dominates even in bulk materials often leading to an order of magnitude or more reduction in the thermal conductivity [35, 52]. Phonon scattering due to mass-disorder in alloys can be written in a similar form to 4.12 as [53]

$$\tau_{mass}^{-1}(\omega) = \frac{\pi S_0}{12} \Gamma_{alloy} \omega^2 D_{2D}(\omega) \ , \tag{4.14}$$

where Γ_{alloy} is the mass-disorder term for alloyed materials and is written as

$$\Gamma_{alloy} = \frac{x(1-x)(m_1 - m_2)^2}{m_{alloy}^2} = \frac{x(1-x)(m_1 - m_2)^2}{[(1-x)m_1 + x m_2]^2} \ . \tag{4.15}$$

Scattering due to alloying is typically stronger than isotope or impurity scattering due to the larger mass-difference $(m_1 - m_2)$ between the constituent materials even at small mixing percentages [52, 53].

Our model also includes phonon scattering due to line-edge roughness and substrate interactions. Phonon collisions with rough boundaries of the 2D layer can be modeled using a 2D variant of the boundary scattering model (See Eqs. 2.8 and 2.9) used in Chapter 2. In this way, phonons collide with the boundary provided they have not already scattered internally where each collision is treated with a momentum-dependent specularity parameter $p(\mathbf{q}) = \exp(-4q^2\Delta\sin^2\theta_B)$. The specularity parameter determines how specular or diffuse the collision event is based on the root-mean-square (rms) roughness Δ, wave-vector $q^2 = ||\mathbf{q}||^2$, and angle of incidence θ_B. Line-edge roughness (LER) scattering can be written as [6, 65]

$$\tau_{LER}^{-1}(\mathbf{q}, j) = \frac{v_\perp(\mathbf{q}, j)}{W} \frac{F_p(\mathbf{q}, j)}{\left[1 - \frac{\Lambda_{int}^{\perp}(\mathbf{q},j)}{W} F_p(\mathbf{q}, j)\right]} \ , \tag{4.16}$$

where W is the width of the nanoribbon, $v_\perp(\mathbf{q}, j)$ are the phonon group velocities perpendicular to the flow of transport (i.e., toward the boundary), and $\Lambda_{int}^{\perp}(\mathbf{q}, j) = v_\perp(\mathbf{q}, j)\tau_{int}^{-1}(\mathbf{q}, j)$ is the phonon mean-free-path perpendicular to the direction of transport. Here, $\tau_{int}^{-1}(\mathbf{q}, j)$ represents the scattering rate of all internal mechanisms; including three-phonon N+U processes, mass-disorder, and substrate interactions when supported. The form factor $F_p(\mathbf{q}, j)$ is written as

$$F_p(\mathbf{q}, j) = \frac{[1 - p(\mathbf{q})]1 - \exp[-W/\Lambda_{int}^{\perp}(\mathbf{q}, j)]}{1 - p(\mathbf{q})\exp[-W/\Lambda_{int}^{\perp}(\mathbf{q}, j)]} \ . \tag{4.17}$$

This model captures the interplay between internal scattering mechanisms and boundary roughness scattering and has been previously used to model line-edge roughness in graphene nanoribbons [6]. Lastly, we also consider the effects of substrate interactions on in-plane transport. For this we follow the work of [93] on the substrate effects on in-plane phonon transport in graphene monolayers, where the substrate scattering rate can be written as

$$\tau_{sub}^{-1}(\omega) = \frac{\pi}{2}\left(\frac{D_{sub}(\omega)}{m_{sub}m_{alloy}} + \frac{D_{2D}(\omega)}{m_{alloy}^2}\right)\frac{K_a^2}{\omega^2} \ . \tag{4.18}$$

In the above, $D_{sub}(\omega)$ is the phonon density of states of the supporting substrate (SiO_2 here), m_{sub} is the mass of atoms on the surface of the substrate, and K_a is the van der Waals (vdW) spring coupling constant. This form of the substrate scattering rate is analogous to the rate used for 2D-3D phonon transport (See Eq. 3.4), however here (for in-plane transport) we assume that the net heat flux across the 2D-3D interface is zero and hence, any phonon that hops from the 2D layer to the substrate must hop back or be replaced by an equivalent phonon from the substrate.

4.2.3 Through-Plane Transport

In addition to studying in-plane phonon transport in TMD alloys, we also study the thermal boundary conductance (TBC) between TMD alloys and a supporting SiO_2 substrate using our 2D-3D interface transport model from Chapter 3. For sake of brevity, the model is identical to the one presented in Sections 3.2.1 and 3.2.2 where we calculate the rate of heat transfer across the 2D-3D interface as a substrate scattering rate written as,

$$\tau_{sub}^{-1}(\omega) = \frac{\pi}{2} \frac{D_{sub}(\omega)}{m_{sub} m_X} \frac{K_a^2}{\omega^2} \ . \tag{4.19}$$

Here, the m_X term represents the atomic mass of chalcogen atoms of the TMD alloy, that is $m_X = m_S, m_{Se}$ for homogeneous TMDs (and for TMD alloys where only the transition metals are mixed) and $m_X = (1-x)m_S + x m_{Se}$ for TMD alloys where the chalcogen atoms are mixed. The phonon density of states of amorphous SiO_2 is extracted from previous molecular dynamics simulations [104]. Also, recall that when a 2D layer is placed on substrate, long-wavelength interactions with the substrate through weak van der Waals forces cause a gapping of the ZA mode. Thus, in calculating the TBC we gap the ZA mode as, $\widetilde{\omega}_{ZA}(\mathbf{q}) = \sqrt{\omega_{ZA}^2(\mathbf{q}) + \omega_0^2}$, where $\omega_0 = \sqrt{\frac{K_a}{m_X}}$ represents the resonant frequency. After the ZA mode is gapped, we calculate the phonon Density of States (pDOS) of the 2D-layer as defined previously (See discussion after Eq. 4.12). Once we calculate the substrate scattering rate and the pDOS of the 2D-layer, we can calculate the TBC as the product of the specific heat and pDOS of the 2D-layer and substrate scattering rate integrated over all phonon energies,

$$G(T) = \frac{Q(T)}{\Delta T} = \int C_{2D}(\omega, T) D_{2D}(\omega) \tau_{sub}^{-1}(\omega) d\omega \; . \tag{4.20}$$

The intriguing aspects of studying the effects of alloying on TBC is within the interplay between the atomic mass m_X in the substrate scattering rate, the gapping of the resonant frequency, and the 2D pDOS.

4.3 Effects of LER and substrate scattering on IP transport

Calculations of room-temperature κ_{IP} for suspended single-layer homogeneous and 50% alloyed TMDs over several orders-of-magnitude in width (W) are shown in Fig. 4.3. The length (L) and rms roughness (Δ) at the line edge are considered to be 100 μm and 0.45 nm, respectively, throughout. Our κ_{IP} predictions for large-sample

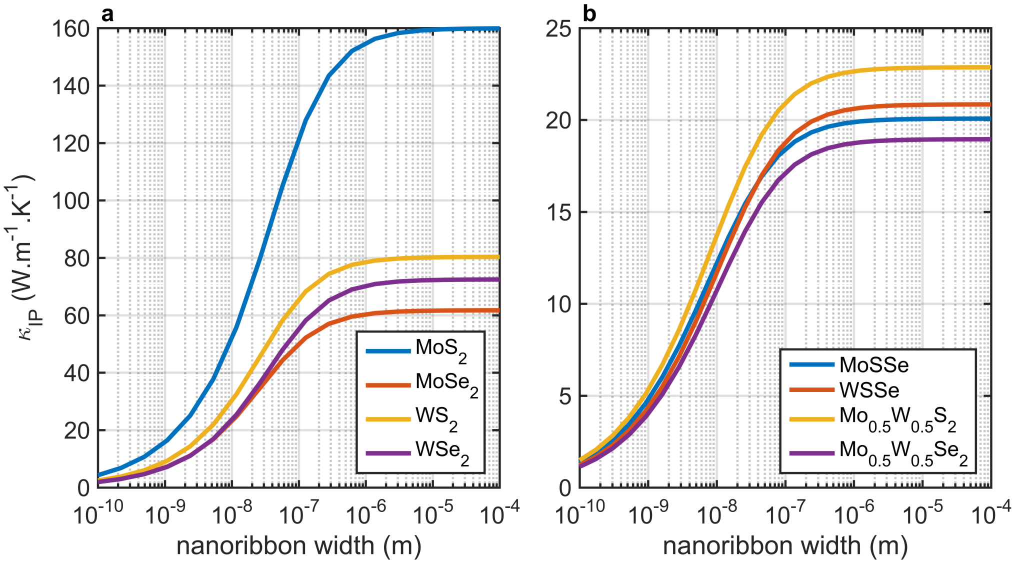

Figure 4.3. The width dependence of in-plane thermal conductivity (κ_{IP}) in the of suspended (a) homogeneous and (b) 50% alloyed TMDs. In either case, transport is considered to be in the zigzag direction with the boundary normals perpendicular to the direction of transport.

homogeneous ($> 10\mu$m in Fig. 4.3a) are within the range of previously reported values but differ in trend for the sulfides. For the four homogeneous TMDs, the bulk in-plane conductivity values are 159, 80.2, 70.5, and 61 W.m^{-1}.K^{-1} for MoS$_2$, WS$_2$, WSe$_2$, and MoSe$_2$, respectively. As width dimensions are scaled down below the 100 nm range, we begin to see a significant reduction in κ_{IP} due to phonon collision with rough line-edges. When the width is scaled down to 5 nm ($\sim$ 15 unit cells across) we see a 75% reduction from the bulk values. Similar size scaling is demonstrated for 50% mixed TMD alloys in Fig. 4.3b, however there are some definitive differences from the homogeneous counterparts.

At large sample dimensions, the 50% mixed TMD alloys show a 3-fold reduction in κ_{IP} ranging from 18.7 W.m^{-1}.K^{-1} in Mo$_{0.5}$W$_{0.5}$Se$_2$ to 22.5 W.m^{-1}.K^{-1} in Mo$_{0.5}$W$_{0.5}$S$_2$ and are in good agreement with values from DFT+PBTE [40] and DFT+pBTE [41]. These values for large-sample alloys, are comparable to the homogeneous nanoribbons with widths smaller than 5 nm. The intrinsically low κ_{IP} for the 50% alloys is further reduced when width-scaling decreases beyond 100 nm, although the decrease is more gradual than in the homogeneous TMDs. The stronger dependence on size-scaling in the homogeneous TMDs lends itself to larger contributions from long mean-free-path (MFP) phonons which collide more readily with the boundary than in the alloys where there are larger contributions from short MFP phonons. Through alloying and nanostructuring our predictions show an order-of-magnitude reduction in κ_{IP} when comparing nanoribbon sized (W<10 nm) TMD alloys to large-sample homogeneous TMDs.

Next, we probe the dependence of κ_{IP} on alloy concentration of suspended and SiO$_2$ supported large-sample (100×100 μm) TMDs in Fig. 4.4a,b. For suspended TMD alloys κ_{IP} we see a steep decline at modest alloying concentrations reaching minimums in the range of 25% to 75% alloy mixing. The values in Fig. 4.4a at 50% alloy mixing are precisely the bulk values presented in Fig. 4.3b. When the

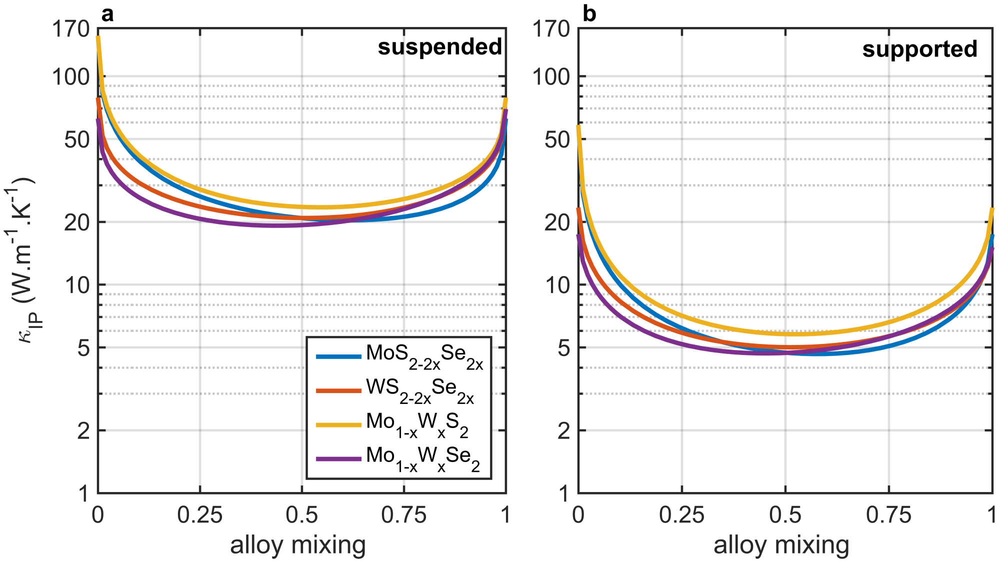

Figure 4.4. The in-plane thermal conductivity of (a) suspended and (b) SiO_2-supported 100×100 μm TMD flakes as a function of alloy mixing. Comparing the suspended and supported flakes, there is a near 3-fold reduction in κ_{IP} of the homogeneous ($x = 0, 1$) SiO_2-supported TMDs, and a further 4-fold reduction in κ_{IP} of 50% ($x = 0.5$) alloyed TMDs.

2D-layers are supported by a SiO_2 substrate, phonon modes (primarily ZA phonons) [93] are dampened by substrate interactions. As a result, the overall scattering of acoustic modes increases leading to a decrease in the in-plane thermal conductivity. For the homogeneous TMDs we see a 3-fold reduction in κ_{IP} across all TMDs. These results for SiO_2-supported single-layer TMDs agree well with measured values of κ_{IP} TMDs supported on a gold-coated SiO_2 substrate handle [118]. When the supported TMDs are alloyed (Fig. 4.4b) we see a similar dependence as the suspended TMDs, where moderate alloying compositions result in a significant reduction in κ_{IP} and a common minimum occurs around 4.6-6 W.m^{-1}.K^{-1}. Predicted values for large-sample SiO_2-supported TMD alloys display very low κ_{IP} comparable to suspended TMD nanoribbons of width less than 2 nm. These significantly low κ_{IP} values for supported large sample size TMD alloys are promising for improved thermoelectric performance.

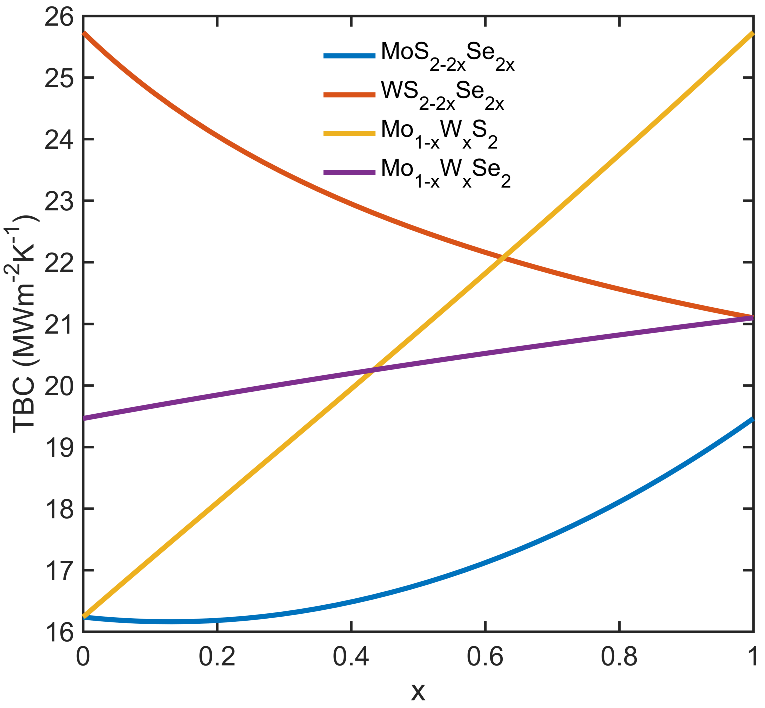

Figure 4.5. Here we show the thermal boundary conductance between select TMD alloys and an SiO_2 substrate as a function of alloy mixing. Compared to the alloy mixing dependence of κ_{IP}, the TBC shows a rather modest alloy composition dependence. The largest and smallest modulation of TBC are +65% and +8.2% along the $Mo_{1-x}W_xS_2$ and $Mo_{1-x}W_xSe_2$ curves, respectively. The value of the vdW coupling constant in these calculations is $K_a = 2.7$ N/m.

4.4 Effects of Alloying on TBC

We also calculated the through-plane thermal boundary conductance (TBC) between TMD alloys and an SiO_2 substrate. In Fig. 4.5 we show TBC as a function of alloy mixing where we see values in the range 16-26 $\mathrm{MW.m^{-2}.K^{-1}}$ which are in good agreement with reported measurements of single-layer MoS_2 on SiO_2 [114, 111]. Our results show a TBC of 25.8, 21.1, 19.5, and 16.3 for WS_2, WSe_2, $MoSe_2$, and MoS_2 on SiO_2, respectively. We find that the trend in TBC across different TMDs depends primarily on variations in atomic mass and phonon spectrum which roll into important features that determine TBC such as the resonant frequency gap, substrate scattering rate, and 2D pDOS. That is, the light atomic mass of the sulfur atoms in WS_2 combined with the lower phonon frequencies caused by the heavier tungsten transition metal maximize Γ_{sub} despite having a larger resonant frequency gap ω_0. With the introduction of Se atoms, although the phonon spectrum decreases (increasing the pDOS at low-frequency) and the resonant frequency gap is lower, the reduction in Γ_{sub} caused by the heavier chalcogen atom causes a net reduction in the TBC. Replacing W atoms with Mo atoms increases the phonon spectrum, thus reducing the pDOS at low-frequency and further decreasing the TBC.

Upon alloying, the TBC values show a qualitatively different trend than in-plane transport and appears to be mostly linear for each TMD alloy, with the exception of $MoS_{2-2x}Se_{2x}$. Additionally, the modulation of TBC values as a function of alloy composition is far weaker than in-plane transport. The largest modulation is seen in $Mo_{1-x}W_xS_2$ which shows a 65% increase in TBC at increasing concentrations of W atoms. On the other hand, small modulation is seen in $Mo_{1-x}W_xSe_2$ showing only a 8.2% increase with increasing concentration of W atoms. In device scenarios where high TBC is required, these results indicate that WS_2 would outperform other TMDs in interface heat transfer. Further, while TBC can be moderately modulated via alloying, the effects are far weaker than in-plane transport. Hence, alloying TMDs may be a useful method for limiting in-plane heat transfer while simultaneously boosting through-plane (TBC) heat removal.

4.5 Chapter Summary

We have investigated the effects of alloying on TMD nanoribbons and suspended and supported micron-sized TMD flakes through a combination of DFPT simulations and phonon Boltzmann transport modeling. Nanostructuring TMDs into nanoribbons we show at least a 3-fold reduction in the thermal conductivity due to line-edge roughness when the ribbon width approaches 5nm. The internal mass-difference scattering imposed through alloying, increases anharmonicty and reduces the thermal conductivity further by at least a factor of 3 compared to the bulk and nanostructured equivalents. We then investigated the effects of substrate interactions on in-plane transport in micron-sized flakes of TMD alloys. Due to the dampening of ZA phonons from substrate interactions we see again a 3-fold (4-fold) reduction in the thermal conductivity from the suspended homogeneous (alloyed) TMDs. Lastly, we studied the effects of alloying on thermal boundary conductance between TMDs and an SiO_2 substrate. Our 2D-3D interface model revealed that the TBC has a qualitatively different trend than in-plane transport as well as a far weaker (nearly linear) dependence on alloy composition. This work helps highlight the importance of line-edge roughness and substrate interactions on the in-plane and through-plane thermal transport of alloyed and non-alloyed TMD 2D-layers.

CHAPTER 5

SUMMARY

In this document we have discussed how modern performance enhancing techniques (strain, nanostructuring, alloying, etc.) affect thermal transport at boundaries and across interfaces through the avenue of three case studies. We used first-principles Density Functional Perturbation Theory to obtain the phonon spectrum of materials of interest and then used the dispersion data as input to semi-classical transport models. In Chapter 2, we investigated the combined effects of strain and boundary scattering on the in-plane and cross-plane thermal conductivity of thin-film silicon and germanium. Our results confirmed a weak strain dependence of the thermal conductivity in the in-plane (IP) direction and uncovered a near ±20% modulation in the cross-plane (CP) direction with ∓4% strain. The contradictory responses between the IP and CP thermal conductivities creates a modulation in the anisotropy between in-plane and cross-plane thermal transport with the application of strain. This modulation was a result of velocity dependent boundary scattering which, in a strongly diffuse regime, depends roughly linearly on velocity. Our results indicated that strain may be an effective tool for modulating the cross-plane thermal conductivity in thin-films for efficient heat removal from strained Si/SOI and Ge/GOI devices. In Chapter 3, we reviewed a recently developed model for cross-dimensional (2D-3D) phonon transport and applied it to 3D-2D-3D stacked interfaces involving graphene and molybdenum disulfide 2D-layers. We showed that an encapsulating layer (atop a 2D-3D interface) can increase the thermal boundary conductance due to surface rayleigh waves in the superstrate which hybridize to monolayer, and thus open an additional pathway for heat to transfer into the substrate. It is also evidenced that softer encapsulating layers, with low transverse sound velocities can improve TBC by adding to the low-frequency pDOS of the 2D-layer. We reveal a roughly quadratic depdence of the TBC on the van der Waals spring coupling between the 2D and 3D materials. This work helps to emphasize the role of adhesion, which is related to the spring coupling, between the monolayer and substrate (or superstrate) as well as the choice of superstrate in influencing the overall cross-plane thermal boundary conductance (TBC) in a 3D-2D-3D stacked system. In Chapter 4, we combined relevant models from Chapters 2 and 3 and studied extrinsic effects, such as line edge roughness and substrate effects, on in-plane and through-plane thermal transport in 1H-phase transition metal dichalcogenide (TMD) alloys. Our results showed that through alloying alone, the lattice thermal conductivity can be significantly reduced even at modest alloying compositions. Further, with the introduction of (extrinsic) atomically rough edges through nanostructuring and substrate effects the thermal conductivity drops by at least another factor of 3 or more. We also show that alloy composition dependence of TBC is modest and qualitatively different than in-plane transport. Our results showed that through the combination of alloying and extrinsic effects one can modulate the in-plane thermal conductivity and through-plane (TBC) conductance of TMD alloys. The former being beneficial for thermoelectric applications which require ultra-low thermal conductivity, and the latter would help improve waste heat removal from hot-spots in the active-layer of 2D-based devices.

APPENDIX

FIRST-PRINCIPLES PHONON SIMULATIONS

A.1 Graphene and MoS_2

The full phonon dispersions of graphene, MoS_2, and Titanium are calculated from first-principles using the open-source suite Quantum-Espresso [37]. Graphene dispersions were obtained using a scalar relativistic norm-conserving pseudopotential (NCPP) which uses a direct-fit Von Barth-Car method with a Perdew-Zunger [81] (LDA) exchange-correlation functional. For MoS_2 we used a non-relativistic NCPP for molybdenum and a scalar relativistic NCPP for sulfur. Both potentials in the MoS2 calculation employed a Martins-Troullier method with a Perdew-Wang [83] (LDA) functional. In order to minimize any interaction between stacked layers, planes of single-layer graphene with planar lattice constant a=2.46 Å or tri-layered S-Mo-S stacked MoS_2 (a=3.125 Å; S-S dist.=3.11 Å) are separated by a 20 Å vacuum. We begin with self-consistent total energy Density Functional Theory (DFT) calculations, with plane wave energy cutoffs of 120 Ry on a Monkhorst-pack (MP) grid size of 12×12×1 for graphene and 140 Ry on a 6×6×4 MP grid for MoS2. After obtaining the eigensystem of electron orbitals and energy states, we use Density Functional Perturbation Theory (DFPT) to obtain the dynamical interatomic force constant matrices [12]. We then inverse Fourier transform the dynamical matrices into real space onto a dense grid of 126,040 q-points, which contains the set of 25,208 equidistant q-points plus grid points for a 2D central difference method around each equidistant point (4×25,208+ 25,208 = 126,040). The phonon group velocities are then calculated from the dispersion data using a central difference method.

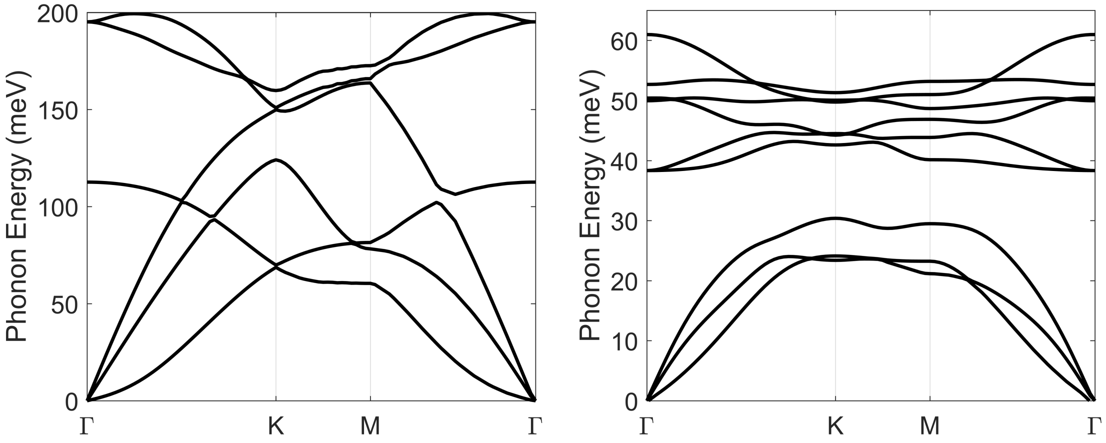

Figure A.1. Phonon dispersion of graphene (left) and MoS_2 (right) from first-principles simulations.

A.2 Titanium

For the phonon dispersion of hexagonal titanium we used a Vanderbilt ultrasoft pseudopotential with a Perdew-Burke-Ernzerhof (GGA) [82] exchange-correlation functional. We relax our unit cell of Ti on a 16×16×16 MP grid with Methfessel-Paxton smearing, a degauss of 0.01 eV and plane wave and charge density energy cutoffs of 50 and 500 Ry, respectively. The system is relaxed until the forces on the atoms are less than 0.0015 eV/Å at which point the lattice constants are a=2.935 Å and c=4.643 Å. After relaxation, we self-consistently calculate the total system energy on a 16×16×16 MP grid. The total energy calculation is then proceeded with a phonon simulation using density functional perturbation theory as implemented in QE [37] on a reduced 4×4×4 MP grid producing the dynamical matrices. We then inverse Fourier transform the dynamical matrices onto real space and extract the phonon frequencies on a dense grid of 176,064 q-points, which contains the set of 25,152 equidistant q-points plus a set of points for a 3D central difference method (25,152 × 6 + 25,152 = 176,064). The resulting dispersion and phonon density of states are presented in Fig. A.2.

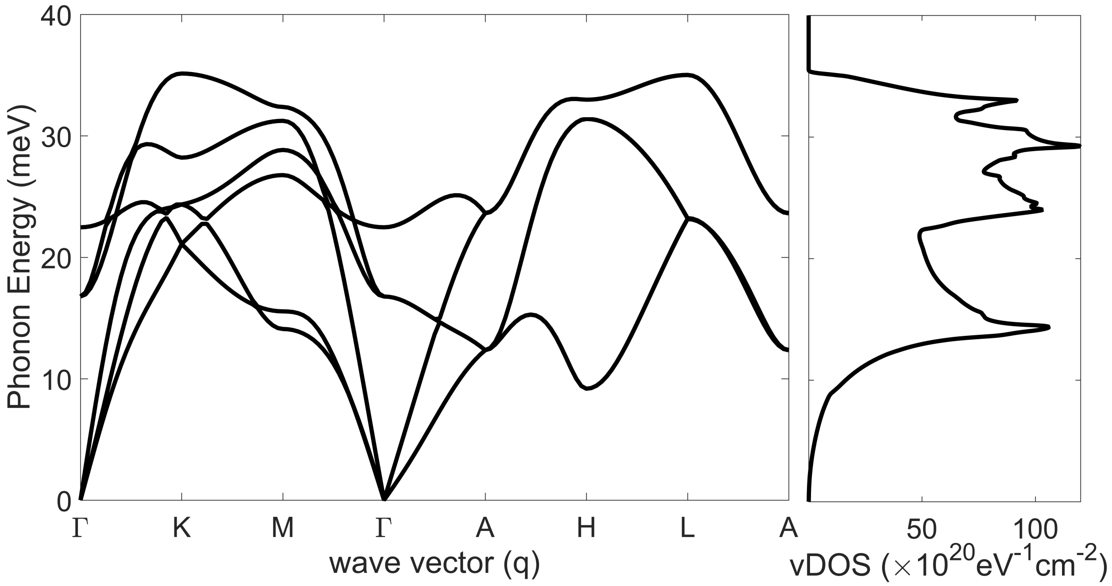

Figure A.2. Phonon dispersion and density of states of Titanium from first-principles simulations.

A.3 MoSe$_2$, WS$_2$, and WSe$_2$

Phonon calculations of single-layer, 1H-phase homogeneous MoSe$_2$, WS$_2$, and WSe$_2$ are performed through density functional perturbation theory [37]. For MoSe$_2$ we used a non-relativistic Martins-Troullier pseudopotential with a PBE/GGA [82] functional. We relax the unit cell structure on an offset 6×6×4 Monkhorst-Pack grid with a plane wave energy cutoff of 140 Ry and a self-consistent field convergence threshold of 10^{-14}. In calculating the phonon dispersion of WS$_2$ and WSe$_2$ we used a scalar relativistic Vanderbilt ultrasoft pseudopotential with a PBE/GGA functional. The structures are relaxed on an offset 27×27×1 and 16×16×1 MP grids for WS$_2$ and WSe$_2$, respectively, with a plane wave energy cutoff of 100 Ry and a self-consistent field convergence threshold of 10^{-14}. All structures are relaxed until the forces on atoms are all less than 5×10^{-4} eV/Å. After structural optimization, we calculate the dynamical matrices using a 6×6×4 Monkhorst-Pack grid for MoSe$_2$ and a 8×8×1 MP grid for both WS$_2$ and WSe$_2$. We then inverse Fourier transform the dynamical matrices into real space onto a dense grid of 126,040 q-points, which contains the set of

25,208 equidistant q-points plus grid points for a 2D central difference method around each equidistant point (4×25,208+ 25,208 = 126,040). The phonon group velocities are then calculated from the dispersion data using a central difference method. The full phonon dispersion obtained from our simulations are shown in Fig. 4.1.

BIBLIOGRAPHY

[1] Aberg, I., Chleirigh, Cait Ni, and Hoyt, J. L. Ultrathin-body strained-si and sige heterostructure-on-insulator mosfets. *IEEE Trans. Electron Devices 53*, 5 (May 2006), 1021–1029.

[2] Akinwande, Deji, Petrone, Nicholas, and Hone, James. Two-dimensional flexible nanoelectronics. *Nat. Commun. 5* (2014).

[3] Aksamija, Z., and Knezevic, I. Anisotropy and boundary scattering in the lattice thermal conductivity of silicon nanomembranes. *Phys. Rev. B 82* (2010), 045319.

[4] Aksamija, Z., and Knezevic, I. Thermoelectric properties of silicon nanostructures. *J. Comput. Electron. 9* (2010), 173.

[5] Aksamija, Z., and Knezevic, I. Anisotropy and edge roughness scattering in the lattice thermal conductivity of graphene nanoribbons. *ECS Transactions 35* (2011), 195.

[6] Aksamija, Z., and Knezevic, I. Lattice thermal conductivity of graphene nanoribbons: anisotropy and edge roughness scattering. *Appl. Phys. Lett. 98* (2011), 141919.

[7] Aksamija, Z., and Knezevic, I. Thermal conductivity of $\mathrm{si}_{1-x}\mathrm{ge}_x/\mathrm{si}_{1-y}\mathrm{ge}_y$ superlattices: Competition between interfacial and internal scattering. *Phys. Rev. B 88* (2013), 155318.

[8] Allen, Philip B. Improved callaway model for lattice thermal conductivity. *Phys. Rev. B 88* (Oct 2013), 144302.

[9] Amorim, Bruno, and Guinea, Francisco. Flexural mode of graphene on a substrate. *Phys. Rev. B 88* (2013), 115418.

[10] Balandin, A. A. Nanophononics: Phonon engineering in nanostructures and nanodevices. *J. Nanosci. Nanotechnol. 5*, 7 (2005), 1.

[11] Balandin, Alexander A., and Nika, Denis L. Phononics in low-dimensional materials. *Materials Today 15*, 6 (2012), 266 – 275.

[12] Baroni, Stefano, de Gironcoli, Stefano, Dal Corso, Andrea, and Giannozzi, Paolo. Phonons and related crystal properties from density-functional perturbation theory. *Rev. Mod. Phys. 73*, 2 (2001), 515–562.

[13] Cahill, D. G., Ford, W. K., Goodson, K. E., Mahan, G. D., Majumdar, A., Maris, H. J., Merlin, R., and Phillipot, S. R. Nanoscale thermal transport. *J. Appl. Phys. 93* (2003), 793–818.

[14] Cahill, David G. Thermal conductivity measurement from 30 to 750 k: the 3ω method. *Review of Scientific Instruments 61*, 2 (1990), 802–808.

[15] Cahill, David G., Braun, Paul V., Chen, Gang, Clarke, David R., Fan, Shanhui, Goodson, Kenneth E., Keblinski, Pawel, King, William P., Mahan, Gerald D., Majumdar, Arun, Maris, Humphrey J., Phillpot, Simon R., Pop, Eric, and Shi, Li. Nanoscale thermal transport. ii. 2003-2012. *Apr. 1*, 1 (2014), 011305.

[16] Cai, Yongqing, Lan, Jinghua, Zhang, Gang, and Zhang, Yong-Wei. Lattice vibrational modes and phonon thermal conductivity of monolayer mos_2. *Phys. Rev. B 89* (2014), 035438.

[17] Callaway, J. Model of lattice thermal conductivity at low temperatures. *Phys. Rev. 113* (1959), 1046–1051.

[18] Chen, G. Size and interface effects on thermal conductivity of superlattices and periodic thin-film structures. *J. Heat. Transfer 119* (1997), 220–229.

[19] Chen, G. Thermal conductivity and ballistic-phonon transport in the cross-plane direction of superlattices. *Phys. Rev. B 57*, 23 (1998), 14958–14973.

[20] Chen, Z., Jang, W., Bao, W., Lau, C. N., and Dames, C. Thermal contact resistance between graphene and silicon dioxide. *Appl. Phys. Lett. 95*, 16 (2009), 161910.

[21] Correa, Gabriela C, Foss, Cameron J, and Aksamija, Zlatan. Interface thermal conductance of van der waals monolayers on amorphous substrates. *Nanotechnology 28*, 13 (2017), 135402.

[22] Cuffe, J., Ristow, O., Chávez, E., Shchepetov, A., Chapuis, P-O., Alzina, F., Hettich, M., Prunnila, M., Ahopelto, J., Dekorsy, T., and Sotomayor Torres, C. M. Lifetimes of confined acoustic phonons in ultrathin silicon membranes. *Phys. Rev. Lett. 110* (2013), 095503.

[23] Cuffe, John, Chvez, Emigdio, Shchepetov, Andrey, Chapuis, Pierre-Olivier, Boudouti, El Houssaine El, Alzina, Francesc, Kehoe, Timothy, Gomis-Bresco, Jordi, Dudek, Damian, Pennec, Yan, Djafari-Rouhani, Bahram, Prunnila, Mika, Ahopelto, Jouni, and Torres, Clivia M. Sotomayor. Phonons in slow motion: Dispersion relations in ultrathin si membranes. *Nano Lett. 12*, 7 (2012), 3569–3573.

[24] Das, Saptarshi, Robinson, Joshua A., Dubey, Madan, Terrones, Humberto, and Terrones, Mauricio. Beyond graphene: Progress in novel two-dimensional materials and van der waals solids. 1–27.

[25] Dettori, Riccardo, Melis, Claudio, Rurali, Riccardo, and Colombo, Luciano. Thermal rectification in silicon by a graded distribution of defects. *J. Appl. Phys. 119*, 21 (2016), 215102.

[26] Dismukes, J. P., Ekstrom, L., Steigmeier, E. F., Kudman, I., and Beers, D. S. Thermal and electrical properties of heavily doped ge-si alloys up to 1300[degree]k. *J. Appl. Phys. 35*, 10 (1964), 2899–2907.

[27] Eryiğit, Resul, and Herman, Irving P. Lattice properties of strained gaas, si, and ge using a modified bond-charge model. *Phys. Rev. B 53*, 12 (1996), 7775–7784.

[28] Esfarjani, Keivan, Chen, Gang, and Stokes, Harold T. Heat transport in silicon from first-principles calculations. *Phys. Rev. B 84* (2011), 085204.

[29] Euaruksakul, C., Li, Z. W., Zheng, F., Himpsel, F. J., Ritz, C. S., Tanto, B., Savage, D. E., Liu, X. S., and Lagally, M. G. Influence of strain on the conduction band structure of strained silicon nanomembranes. *Phys. Rev. Lett. 101* (2008), 147403.

[30] Evans, William J., Hu, Lin, and Keblinski, Pawel. Thermal conductivity of graphene ribbons from equilibrium molecular dynamics: Effect of ribbon width, edge roughness, and hydrogen termination. *Appl. Phys. Lett. 96*, 20 (2010), 203112.

[31] Fang, Tian, Konar, Aniruddha, Xing, Huili, and Jena, Debdeep. Mobility in semiconducting graphene nanoribbons: Phonon, impurity, and edge roughness scattering. *Phys. Rev. B 78* (2008), 205403.

[32] Feng, Qingliang, Zhu, Yiming, Hong, Jinhua, Zhang, Mei, Duan, Wenjie, Mao, Nannan, Wu, Juanxia, Xu, Hua, Dong, Fengliang, Lin, Fang, Jin, Chuanhong, Wang, Chunming, Zhang, Jin, and Xie, Liming. Growth of large-area 2d $\mathrm{mos}_{2(1-x)}\mathrm{se}_{2x}$ semiconductor alloys. *Advanced Materials 26*, 17 (2014), 2648–2653.

[33] Fischetti, M. V., and Laux, S. E. Band structure, deformation potentials, and carrier mobility in strained si, ge, and sige alloys. *J. Appl. Phys. 80*, 4 (1996), 2234–2252.

[34] Foss, C. J., and Aksamija, Z. Strain effects on thermal transport and anisotropy in thin-films of si and ge. *J. Appl. Phys. 120* (2016), 225104.

[35] Garg, Jivtesh, Bonini, Nicola, Kozinsky, Boris, and Marzari, Nicola. Role of disorder and anharmonicity in the thermal conductivity of silicon-germanium alloys: A first-principles study. *Phys. Rev. Lett. 106* (Jan 2011), 045901.

[36] Geim, A. K. Graphene: Status and Prospects. *Science 324*, 5934 (2009), 1530–1534.

[37] Giannozzi, Paolo, Baroni, Stefano, Bonini, Nicola, Calandra, Matteo, Car, Roberto, Cavazzoni, Carlo, Ceresoli, Davide, Chiarotti, Guido L, Cococcioni, Matteo, Dabo, Ismaila, Dal Corso, Andrea, de Gironcoli, Stefano, Fabris, Stefano, Fratesi, Guido, Gebauer, Ralph, Gerstmann, Uwe, Gougoussis, Christos, Kokalj, Anton, Lazzeri, Michele, Martin-Samos, Layla, Marzari, Nicola, Mauri, Francesco, Mazzarello, Riccardo, Paolini, Stefano, Pasquarello, Alfredo, Paulatto, Lorenzo, Sbraccia, Carlo, Scandolo, Sandro, Sclauzero, Gabriele, Seitsonen, Ari P, Smogunov, Alexander, Umari, Paolo, and Wentzcovitch, Renata M. Quantum espresso: a modular and open-source software project for quantum simulations of materials. *Journal of Physics: Condensed Matter 21*, 39 (2009), 395502.

[38] Gilat, G., and Raubenheimer, L. J. Accurate numerical method for calculating frequency-distribution functions in solids. *Phys. Rev. 144*, 2 (1966), 390–395.

[39] Gu, Xiaokun, and Yang, Ronggui. Phonon transport in single-layer transition metal dichalcogenides: A first-principles study. *Appl. Phys. Lett. 105*, 13 (2014), 131903.

[40] Gu, Xiaokun, and Yang, Ronggui. Phonon transport in single-layer $\mathrm{mo}_{1-x}\mathrm{w}_x\mathrm{s}_2$ alloy embedded with ws_2 nanodomains. *Phys. Rev. B 94*, 7 (Aug 2016).

[41] Guo, San-Dong. Phonon transport in janus monolayer mosse: a first-principles study. *Phys. Chem. Chem. Phys. 20* (2018), 7236–7242.

[42] Henry, A. S., and Chen, G. Spectral phonon transport properties of silicon based on molecular dynamics simulations and lattice dynamics. *J. Comput. Theor. Nanosci. 5* (2008), 1–12.

[43] Hinsche, N F, Mertig, I, and Zahn, P. Effect of strain on the thermoelectric properties of silicon: an abinitio study. *J. Phys.: Condens. Matter 23*, 29 (2011), 295502.

[44] Hong, Yang, Zhang, Jingchao, and Zeng, Xiao Cheng. Thermal conductivity of monolayer mose2 and mos2. *J. Phys. Chem. 120*, 45 (2016), 26067–26075.

[45] Hopkins, Patrick E., Duda, John C., and Norris, Pamela M. Anharmonic phonon interactions at interfaces and contributions to thermal boundary conductance. *J. Heat Transf. 133* (2011), 062401.

[46] Hua, Chengyun, Chen, Xiangwen, Ravichandran, Navaneetha K., and Minnich, Austin J. Experimental metrology to obtain thermal phonon transmission coefficients at solid interfaces. *Phys. Rev. B 95* (2017), 205423.

[47] Huang, Huaqing, Xu, Yong, Zou, Xiaolong, Wu, Jian, and Duan, Wenhui. Tuning thermal conduction via extended defects in graphene. *Phys. Rev. B 87* (2013), 205415.

[48] Huang, Minghuang, Ritz, Clark S., Novakovic, Bozidar, Yu, Decai, Zhang, Yu, Flack, Frank, Savage, Donald E., Evans, Paul G., Knezevic, Irena, Liu, Feng, and Lagally, Max G. Mechano-electronic superlattices in silicon nanoribbons. *ACS Nano 3* (2009), 721–727.

[49] Jain, Jinendra Raja, Hryciw, Aaron, Baer, Thomas M., Miller, David A. B., Brongersma, Mark L., and Howe, Roger T. A micromachining-based technology for enhancing germanium light emission via tensile strain. *Nature Photonics 6* (2012), 398–405.

[50] Jariwala, Deep, Sangwan, Vinod K., Lauhon, Lincoln J., Marks, Tobin J., and Hersam, Mark C. Emerging device applications for semiconducting two-dimensional transition metal dichalcogenides. *ACS Nano 8*, 2 (2014), 1102–1120.

[51] Jiang, Puqing, Qian, Xin, Gu, Xiaokun, and Yang, Ronggui. Probing anisotropic thermal conductivity of transition metal dichalcogenides mx2 (m = mo, w and x = s, se) using time-domain thermoreflectance. *Adv. Mater. 29*, 36 (9 2017).

[52] Ju, James, Sun, Bo, Haunschild, Georg, Loitsch, Bernhard, Stoib, Benedikt, Brandt, Martin S., Stutzmann, Martin, Koh, Yee Kan, and Koblmller, Gregor. Thermoelectric properties of in-rich ingan and inn/ingan superlattices. *AIP Advances 6*, 4 (2016), 045216.

[53] Khatami, S. N., and Aksamija, Z. Lattice thermal conductivity of the binary and ternary group-iv alloys si-sn, ge-sn, and si-ge-sn. *Phys. Rev. Applied 6* (2016), 014015.

[54] Kim, Seung-Yoon, Choi, Sung-Yool, Hwang, Wan Sik, and Cho, Byung Jin. Valley-engineered ultra-thin silicon for high-performance junctionless transistors. *Scientific Reports 6* (2016), 29354.

[55] Klemens, P. G. Thermal resistance due to point defects at high temperatures. *Phys. Rev. 119*, 2 (1960), 507–509.

[56] Koga, T., Sun, X., Cronin, S. B., and Dresselhaus, M. S. Carrier pocket engineering applied to “strained” si/ge superlattices to design useful thermoelectric materials. *Appl. Phys. Lett. 75*, 16 (1999), 2438–2440.

[57] Koh, Yee Kan, Lyons, Austin S., Bae, Myung-Ho, Huang, Bin, Dorgan, Vincent E., Cahill, David G., and Pop, Eric. Role of remote interfacial phonon (rip) scattering in heat transport across graphene/sio$_2$ interfaces. *Nano Lett.* (2016).

[58] Larkin, Jason M., and McGaughey, Alan J. H. Predicting alloy vibrational mode properties using lattice dynamics calculations, molecular dynamics simulations, and the virtual crystal approximation. *J. Appl. Phys. 114*, 2 (2013), 023507.

[59] Lewis, J. E., Rodot, H., and Haen, P. The low-temperature thermoelectric power and thermal conductivity of gete and of some gete-mnte alloys. *physica status solidi (b) 29*, 2 (1968), 743–754.

[60] Li, Xiaobo, Maute, Kurt, Dunn, Martin L., and Yang, Ronggui. Strain effects on the thermal conductivity of nanostructures. *Phys. Rev. B 81* (Jun 2010), 245318.

[61] Li, Yao, Duerloo, Karel-Alexander N, Wauson, Kerry, and Reed, Evan J. Structural semiconductor-to-semimetal phase transition in two-dimensional materials induced by electrostatic gating. *Nat Commun 7* (2016), ncomms10671.

[62] Little, W. A. The transport of heat between dissimilar solids at low temperatures. *Canadian Journal of Physics 37*, 3 (1959), 334–349.

[63] Liu, Weili, and Balandin, Alexander A. Thermal conduction in alxga1xn alloys and thin films. *J. Appl. Phys. 97* (2005), 073710.

[64] Lu, Ziyang, Layani, Michael, Zhao, Xiaoxu, Tan, Li Ping, Sun, Ting, Fan, Shufen, Yan, Qingyu, Magdassi, Shlomo, and Hng, Huey Hoon. Fabrication of flexible thermoelectric thin film devices by inkjet printing. *Small 10*, 17 (2014), 3551–3554.

[65] Majee, Arnab K., and Aksamija, Zlatan. Length divergence of the lattice thermal conductivity in suspended graphene nanoribbons. *Phys. Rev. B 93* (2016), 235423.

[66] Malhotra, Abhinav, and Maldovan, Martin. Impact of phonon surface scattering on thermal energy distribution of si and sige nanowires. *Sci. Rep. 6* (2016), 25818.

[67] Maris, Humphrey J. Phonon propagation with isotope scattering and spontaneous anharmonic decay. *Phys. Rev. B 41*, 14 (1990), 9736–9743.

[68] Martin, Pierre N., Aksamija, Zlatan, Pop, Eric, and Ravaioli, Umberto. Reduced thermal conductivity in nanoengineered rough ge and gaas nanowires. *Nano Lett. 10* (2010), 1120–1124.

[69] McCurdy, A. K., Maris, H. J., and Elbaum, C. Anisotropic heat conduction in cubic crystals in the boundary scattering regime. *Phys. Rev. B 2*, 10 (1970), 4077–4083.

[70] Mei, S., Foss, C. J., Maurer, L. N., Jonasson, O., Aksamija, Z., and Knezevic, I. Boundaries, interfaces, point defects, and strain as impediments to thermal transport in nanostructures. In *2017 IEEE International Reliability Physics Symposium (IRPS)* (April 2017), pp. 6A–1.1–6A–1.10.

[71] Moore, Arden L., and Shi, Li. Emerging challenges and materials for thermal management of electronics. *Materials Today 17*, 4 (2014), 163 – 174.

[72] Morelli, D. T., Heremans, J. P., and Slack, G. A. Estimation of the isotope effect on the lattice thermal conductivity of group IV and group III-V semiconductors. *Phys. Rev. B 66*, 19 (2002), 195304.

[73] Murphy, Kathryn F., Piccione, Brian, Zanjani, Mehdi B., Lukes, Jennifer R., and Gianola, Daniel S. Strain- and defect-mediated thermal conductivity in silicon nanowires. *Nano Lett. 14*, 7 (2014), 3785–3792.

[74] Nika, D. L., Pokatilov, E. P., Askerov, A. S., and Balandin, A. A. Phonon thermal conduction in graphene: Role of umklapp and edge roughness scattering. *Phys. Rev. B 79*, 15 (2009), 155413.

[75] Novoselov, K. S., Geim, A. K., Morozov, S. V., Jiang, D., Katsnelson, M. I., Grigorieva, I. V., Dubonos, S. V., and Firsov, A. A. Two-dimensional gas of massless dirac fermions in graphene. *Nature 438*, 7065 (2005), 197–200.

[76] Novoselov, K. S., Geim, A. K., Morozov, S. V., Jiang, D., Zhang, Y., Dubonos, S. V., Grigorieva, I. V., and Firsov, A. A. Electric field effect in atomically thin carbon films. *Science 306*, 5696 (2004), 666–669.

[77] Ong, Zhun-Yong, Cai, Yongqing, and Zhang, Gang. Theory of substrate-directed heat dissipation for single-layer graphene and other two-dimensional crystals. *Phys. Rev. B 94* (2016), 165427.

[78] Paul, Abhijeet, and Klimeck, Gerhard. Strain effects on the phonon thermal properties of ultra-scaled si nanowires. *Appl. Phys. Lett. 99*, 8 (2011), 083115.

[79] Peimyoo, Namphung, Shang, Jingzhi, Yang, Weihuang, Wang, Yanlong, Cong, Chunxiao, and Yu, Ting. Thermal conductivity determination of suspended mono- and bilayer ws2 by raman spectroscopy. *Nano Research 8*, 4 (2015), 1210–1221.

[80] Peng, Bo, Zhang, Hao, Shao, Hezhu, Xu, Yuchen, Zhang, Xiangchao, and Zhu, Heyuan. Thermal conductivity of monolayer mos2, mose2, and ws2: interplay of mass effect, interatomic bonding and anharmonicity. *RSC Adv. 6* (2016), 5767–5773.

[81] Perdew, J. P., and Zunger, Alex. Self-interaction correction to density-functional approximations for many-electron systems. *Phys. Rev. B 23* (May 1981), 5048–5079.

[82] Perdew, John P., Burke, Kieron, and Ernzerhof, Matthias. Generalized gradient approximation made simple. *Phys. Rev. Lett. 77* (Oct 1996), 3865–3868.

[83] Perdew, John P., and Wang, Yue. Accurate and simple analytic representation of the electron-gas correlation energy. *Phys. Rev. B 45* (Jun 1992), 13244–13249.

[84] Persson, B. N. J., and Ueba, H. Heat transfer between weakly coupled systems: Graphene on a-sio 2. *Europhys. Lett. 91* (2010), 56001.

[85] Pop, E., Sinha, S., and Goodson, K.E. Heat generation and transport in nanometer-scale transistors. In *Proc. IEEE* (2006), vol. 94, pp. 1587–1601.

[86] Prasher, Ravi. Acoustic mismatch model for thermal contact resistance of van der waals contacts. *Appl. Phys. Lett. 94*, 4 (2009), 041905.

[87] Prasher, Ravi, Tong, Tao, and Majumdar, Arun. Approximate analytical models for phonon specific heat and ballistic thermal conductance of nanowires. *Nano Lett. 8*, 1 (2008), 99–103.

[88] Qian, Xin, Jiang, Puqing, Yu, Peng, Gu, Xiaokun, Liu, Zheng, and Yang, Ronggui. Anisotropic thermal transport in Phase-Transition layered 2D alloys WSe2(1-x)Te2x. *https://arxiv.org/abs/1802.10009* (2018).

[89] Qteish, A., and Molinari, E. Interplanar forces and phonon spectra of strained si and ge: Ab initio calculations and applications to si/ge superlattices. *Phys. Rev. B 42*, 11 (1990), 7090–7096.

[90] Rieger, Martin M., and Vogl, P. Electronic-band parameters in strained $si_{1-x}ge_x$ alloys on $si_{1-y}ge_y$ substrates. *Phys. Rev. B 48*, 19 (1993), 14276–14287.

[91] Schroeder, D. P., Aksamija, Z., Rath, A., Voyles, P. M., Lagally, M. G., and Eriksson, M. A. Thermal resistance of transferred-silicon-nanomembrane interfaces. *Phys. Rev. Lett. 115* (2015), 256101.

[92] Schwierz, F., Pezoldt, J., and Granzner, R. Two-dimensional materials and their prospects in transistor electronics. *Nanoscale 7* (2015), 8261–8283.

[93] Seol, Jae Hun, Jo, Insun, Moore, Arden L., Lindsay, Lucas, Aitken, Zachary H., Pettes, Michael T., Li, Xuesong, Yao, Zhen, Huang, Rui, Broido, David, Mingo, Natalio, Ruoff, Rodney S., and Shi, Li. Two-dimensional phonon transport in supported graphene. *Science 328*, 5975 (2010), 213–216.

[94] Snchez-Prez, Jose R., Boztug, Cicek, Chen, Feng, Sudradjat, Faisal F., Paskiewicz, Deborah M., Jacobson, RB, Lagally, Max G., and Paiella, Roberto. Direct-bandgap light-emitting germanium in tensilely strained nanomembranes. *Proceedings of the National Academy of Sciences 108*, 47 (2011), 18893–18898.

[95] Sui, Zhifeng, and Herman, Irving P. Effect of strain on phonons in si, ge, and si/ge heterostructures. *Phys. Rev. B 48*, 24 (1993), 17938–17953.

[96] Swartz, E. T., and Pohl, R. O. Thermal resistance at interfaces. *Appl. Phys. Lett. 51* (1987), 200.

[97] Swartz, E. T., and Pohl, R. O. Thermal boundary resistance. *Rev. Mod. Phys. 61*, 3 (1989), 605–668.

[98] Taleb, Amjad Al, and Faras, Daniel. Phonon dynamics of graphene on metals. *J. Phys.: Condens. Matter 28*, 10 (2016), 103005.

[99] Tamura, S., Shields, J. A., and Wolfe, J. P. Lattice dynamics and elastic phonon scattering in silicon. *Phys. Rev. B 44* (1991), 3001.

[100] Tamura, Shin-Ichiro. Isotope scattering of dispersive phonons in Ge. *Phys. Rev. B 27*, 2 (1983), 858–866.

[101] Uma, S., McConnell, A. D., Asheghi, M., Kurabayashi, K., and Goodson, K. E. Temperature-dependent thermal conductivity of undoped polycrystalline silicon layers. *International Journal of Thermophysics 22* (2001), 605–616.

[102] Upadhyaya, Meenakshi, Khatami, Seyedeh Nazanin, and Aksamija, Zlatan. Engineering thermal transport in sige-based nanostructures for thermoelectric applications. *J. Mater. Res. 30* (2015), 2649–2662.

[103] Volz, Sebastian, Ordonez-Miranda, Jose, Shchepetov, Andrey, Prunnila, Mika, Ahopelto, Jouni, Pezeril, Thomas, Vaudel, Gwenaelle, Gusev, Vitaly, Ruello, Pascal, Weig, Eva M., Schubert, Martin, Hettich, Mike, Grossman, Martin, Dekorsy, Thomas, Alzina, Francesc, Graczykowski, Bartlomiej, Chavez-Angel, Emigdio, Sebastian Reparaz, J., Wagner, Markus R., Sotomayor-Torres, Clivia M., Xiong, Shiyun, Neogi, Sanghamitra, and Donadio, Davide. Nanophononics: state of the art and perspectives. *The European Physical Journal B 89*, 1 (2016), 15.

[104] Wang, C., Tamai, Y., and Kuzuu, N. A molecular dynamics study on vibration spectra of a-sio$_2$ surface. *Journal of Non-Crystalline Solids 321* (2003), 204–209.

[105] Wang, Xinjiang, and Huang, Baoling. Computational study of in-plane phonon transport in si thin films. *Sci. Rep.* (2014).

[106] Wang, Yan, Qiu, Bo, and Ruan, Xiulin. Edge effect on thermal transport in graphene nanoribbons: A phonon localization mechanism beyond edge roughness scattering. *Appl. Phys. Lett. 101*, 1 (2012), 013101.

[107] Wang, Yuxi, Xu, Ning, Li, Deyu, and Zhu, Jia. Thermal properties of two dimensional layered materials. *Adv. Func. Mater.* (2017), 1604134.

[108] Ward, A., and Broido, D. A. Intrinsic phonon relaxation times from first-principles studies of the thermal conductivities of Si and Ge. *Phys. Rev. B 81*, 8 (2010), 085205.

[109] Xia, Fengnian, Wang, Han, Xiao, Di, Dubey, Madan, and Ramasubramaniam, Ashwin. Two-dimensional material nanophotonics. *Nat Photon 8*, 12 (Dec. 2014), 899–907.

[110] Xu, Y., and Li, G. Strain effect analysis on phonon thermal conductivity of two-dimensional nanocomposites. *J. Appl. Phys. 106*, 11 (2009), 114302.

[111] Yalon, Eilam, McClellan, Connor J., Smithe, Kirby K. H., Muoz Rojo, Miguel, Xu, Runjie Lily, Suryavanshi, Saurabh V., Gabourie, Alex J., Neumann, Christopher M., Xiong, Feng, Farimani, Amir Barati, and Pop, Eric. Energy dissipation in monolayer mos2 electronics. *Nano Letters 17*, 6 (2017), 3429–3433.

[112] Yan, Rusen, Simpson, Jeffrey R., Bertolazzi, Simone, Brivio, Jacopo, Watson, Michael, Wu, Xufei, Kis, Andras, Luo, Tengfei, Hight Walker, Angela R., and Xing, Huili Grace. Thermal conductivity of monolayer molybdenum disulfide obtained from temperature-dependent raman spectroscopy. *ACS Nano 8* (2014), 986–993.

[113] Yang, Juekuan, Yang, Yang, Waltermire, Scott W., Wu, Xiaoxia, Zhang, Haitao, Gutu, Timothy, Jiang, Youfei, Chen, Yunfei, Zinn, Alfred A., Prasher, Ravi, Xu, Terry T., and Li, Deyu. Enhanced and switchable nanoscale thermal conduction due to van der waals interfaces. *Nat Nano 7*, 2 (2012), 91–95.

[114] Yasaei, Poya, Foss, Cameron J., Karis, Klas, Behranginia, Amirhossein, El-Ghandour, Ahmed I., Fathizadeh, Arman, Olivares, Javier, Majee, Arnab K., Foster, Craig D., Khalili-Araghi, Fatemeh, Aksamija, Zlatan, and Salehi-Khojin, Amin. Interfacial thermal transport in monolayer mos2- and graphene-based devices. *Advanced Materials Interfaces 4*, 17 (2017), 1700334–n/a. 1700334.

[115] Yazyev, Oleg V., and Louie, Steven G. Topological defects in graphene: Dislocations and grain boundaries. *Phys. Rev. B 81*, 19 (2010), 195420.

[116] Yuea, Yanan, Zhang, Jingchao, Tang, Xiaoduan, Xu, Shen, and Wang, Xinwei. Thermal transport across atomic-layer material interfaces. *Nanotechnol. Rev. 4*, 6 (2015), 533–555.

[117] Zhang, Jing, Jia, Shuai, Kholmanov, Iskandar, Dong, Liang, Er, Dequan, Chen, Weibing, Guo, Hua, Jin, Zehua, Shenoy, Vivek B., Shi, Li, and Lou, Jun. Janus monolayer transition-metal dichalcogenides. *ACS Nano 11*, 8 (2017), 8192–8198.

[118] Zhang, Xian, Sun, Dezheng, Li, Yilei, Lee, Gwan-Hyoung, Cui, Xu, Chenet, Daniel, You, Yumeng, Heinz, Tony F., and Hone, James C. Measurement of lateral and interfacial thermal conductivity of single- and bilayer mos2 and mose2 using refined optothermal raman technique. *ACS Applied Materials & Interfaces 7*, 46 (2015), 25923–25929.

[119] Zhang, Xingli, and Wu, Guoqiang. Effect of strain on thermal conductivity of silicon thin films. *Journal of Nanomaterials* (2016).

[120] Zhang, Zhongwei, Xie, Yuee, Ouyang, Yulou, and Chen, Yuanping. A systematic investigation of thermal conductivities of transition metal dichalcogenides. *Int. J. Heat Mass Transfer 108* (2017), 417 – 422.

[121] Zhu, Jie, Tang, Dawei, Wang, Wei, Liu, Jun, Holub, Kristopher W., and Yang, Ronggui. Ultrafast thermoreflectance techniques for measuring thermal conductivity and interface thermal conductance of thin films. *J. Appl. Phys. 108*, 9 (2010), 094315.